LA-UR-23-25233
NP3M-P2300016

Maximally local two-nucleon interactions at fourth order in delta-less chiral effective field theory

R. Somasundaram,[1,2,*] J.E. Lynn,[1,3,4] L. Huth,[3,4] A. Schwenk,[3,4,5] and I. Tews[1,†]

[1] *Theoretical Division, Los Alamos National Laboratory, Los Alamos, New Mexico 87545, USA*
[2] *Department of Physics, Syracuse University, Syracuse, NY 13244, USA*
[3] *Technische Universität Darmstadt, Department of Physics, 64289 Darmstadt, Germany*
[4] *ExtreMe Matter Institute EMMI, GSI Helmholtzzentrum für Schwerionenforschung GmbH, 64291 Darmstadt, Germany*
[5] *Max-Planck-Institut für Kernphysik, Saupfercheckweg 1, 69117 Heidelberg, Germany*

(Dated: June 26, 2023)

We present new maximally-local two-nucleon interactions derived in delta-less chiral effective field theory up to next-to-next-to-next-to leading order that include all contact and pion-exchange contributions to the nuclear Hamiltonian up to this order. Our interactions are fit to nucleon-nucleon phase shifts using a Bayesian statistical approach, and explore a wide cutoff range from $0.6-0.9$ fm (~ 440 MeV to ~ 660 MeV). These interactions can be straightforwardly employed in accurate quantum Monte Carlo methods, such as the auxiliary field diffusion Monte Carlo method. Together with local three-nucleon forces, calculations with these new interactions will provide improved benchmarks for the structure of atomic nuclei and serve as crucial input to analyses of exciting astrophysical phenomena involving neutron stars, such as binary neutron-star mergers.

I. INTRODUCTION

Violent astrophysical explosions involving neutron stars (NSs), like supernovae and NS mergers, are fascinating phenomena to study for nuclear physics. NSs and their mergers explore nuclear matter reaching the highest densities in the cosmos, making them ideal laboratories to elucidate strong nuclear interactions. These interactions manifest themselves in the form of the nuclear-matter equation of state (EOS), which connects NSs with nuclear experiments, e.g., at the Facility for Rare Isotope Beams (FRIB) or the Relativistic Heavy-Ion Collider (RHIC). Recently, exciting multi-messenger analyses, combining state-of-the-art nuclear theory with exciting astrophysical data, have provided a wealth of new information on the EOS [1–8]. These analyses used constraints on the EOS of dense matter that were obtained from many-body calculations using interactions from chiral effective field theory (EFT) [9–11]. Chiral EFT provides a systematic expansion of nuclear interactions and is connected to the fundamental theory of strong interactions, quantum Chromodynamics. While there has been a lot of progress in recent years to improve chiral EFT constraints, it is crucial to reduce uncertainties of theoretical models for nuclear interactions to fully exploit the multitude of anticipated data from NS observations and nuclear experiments in the coming years.

One way to achieve this goal is to perform calculations at higher orders in the chiral EFT expansion. In this paper, we introduce a new family of local chiral EFT two-nucleon (NN) interactions at next-to-next-to-next-to-leading order ($\mathrm{N^3LO}$) that can be employed in quantum Monte Carlo (QMC) computational methods. QMC methods are among the most precise and accurate many-body methods [12] but they require local interactions as input. In the past, local interactions from chiral EFT have been developed up to next-to-next-to-leading order ($\mathrm{N^2LO}$) in the delta-less approach [13, 14] and, including short-range pieces at $\mathrm{N^3LO}$, in the delta-full approach [15, 16]. Fully-local chiral interactions have also recently been developed in the delta-less approach where all available local operators up to $\mathrm{N^3LO}$ were considered, even those that would be connected by antisymmetrization and the Fierz rearrangement freedom (FRF) [17]. In particular, four leading-order (LO) operators, 8 local next-to-leading order (NLO) operators, and all 11 local $\mathrm{N^3LO}$ operators were considered while all nonlocal pieces and their associated physics were not included.

Here, instead, we will develop maximally local interactions for use in QMC methods while using FRF [18]. Local chiral EFT interactions up to $\mathrm{N^2LO}$, developed following our approach, have been used in QMC methods and provide a good description of atomic nuclei with $A \lesssim 20$ [19, 20] and dense matter [21–23]. However, uncertainties in these calculations are still sizable and result from both the truncation of the chiral series and regulator artifacts. These uncertainties limit inferences of, e.g., differences in charge radii of mirror nuclei that can be connected with the neutron-skin thickness of lead [24], which was recently inferred from measurements by the PREX collaboration [25] and has been used to constrain the EOS [6, 26, 27]. Similarly, present uncertainties affect estimations of the nuclear symmetry energy and other properties of dense matter [23]. Forthcoming astrophysics constraints from gravitational-wave (GW) observatories will provide precision data on dense matter [28] and it is key that uncertainties in many-body calculations at low densities are reduced to enable best-possible analyses of these exciting new data. Here, we focus on developing novel maximally local $\mathrm{N^3LO}$ NN interactions that can be straightforwardly used in QMC calculations

* rsomasun@syr.edu
† itews@lanl.gov

of various nuclear systems. In a forthcoming paper, we will include the parameter-free N^{3}LO three-nucleon (3N) interactions [29, 30], the charge-symmetry and charge-independence breaking corrections, and full QMC calculations of many-body nuclear systems. Calculations at higher orders in the EFT expansion are expected to reduce theoretical uncertainties by a factor of ~ 2 [31].

The interactions developed here include a set of 21 contact operators, out of which 4 are nonlocal. All pion-exchange interactions are local and fully included in the Hamiltonian. The local interactions developed here explore a wide range of cutoffs, $R_0 = 0.6 - 0.9$ fm ($\sim$ 440 MeV to $\sim$ 660 MeV), in order to reduce the impact of regulator artifacts. This is an important aspect of our calculation since previous studies have shown that regulator artifacts from local regulators are larger than for nonlocal regulators [18, 21, 32]. High-cutoff interactions have smaller regulator artifacts and can easily be employed in QMC calculations, in contrast to most other many-body methods that require softened interactions for convergence. Our N^{3}LO interactions, which we name N^{3}LO$_{\rm LA}$-09 to N^{3}LO$_{\rm LA}$-06, are fit to NN scattering phase shifts using the method of Bayesian inference. This allows us to explicitly model EFT truncation uncertainties when performing the fits and we show how these uncertainties evolve with the cutoff R_0. We also perform least-squares fits to the NN scattering phase shifts that do not incorporate EFT truncation uncertainties. The comparison between the two ways of fitting indicates the importance of modeling the EFT truncation uncertainties when chiral interactions are calibrated to data. We demonstrate that local high-cutoff (hard core) interactions perform better than their softer counterparts, in the sense that they better reproduce NN scattering phase shifts and lead to smaller EFT truncation uncertainties. Finally, we show that although our interactions are not fit to the properties of the deuteron, our model predictions for these are in good agreement with experimental data, especially for our high-cutoff interactions.

This paper is organized as follows. In Sec. II, we give the explicit form of the Hamiltonian that we use in this work. The couplings of this Hamiltonian are fit to NN scattering phase shifts and the details of this fit are given in Sec. III, where we discuss both the Bayesian fit as well as the least-squares fit. We also show how the np phase shifts and their associated theoretical uncertainties change with increasing the chiral order and varying the cutoff. In Sec. IV, we use our interactions to study the properties of the deuteron. Our main conclusions and summary are presented in Sec. V

II. N^{3}LO HAMILTONIAN FROM CHIRAL EFT

In this section, we give the detailed expressions for the Hamiltonian along with the local regulators that we have employed in this work. Since there are four nonlocal contact operators in our Hamiltonian, we present the momentum-space expression for all the contacts that we use. The pion-exchange terms and the local regulators, on the other hand, are treated in coordinate space.

A. Chiral EFT and QMC methods

In atomic nuclei and nuclear matter below about twice the nuclear saturation density, chiral EFT is currently the main framework to describe nuclear interactions in a systematic order-by-order expansion [9–11]. The chiral EFT framework provides consistent NN, 3N, and multi-nucleon interactions, based on a low-momentum expansion of nuclear forces in powers of the nucleons' momenta Q over the breakdown scale Λ_b, which determines where chiral EFT becomes inapplicable. High-momentum processes, that would be resolved at momenta above the breakdown scale, are absorbed into a set of coupling constants, the strengths of which are adjusted to reproduce experimental data. The advantages of chiral EFT over other approaches are that it (i) allows us to quantify theoretical uncertainties [31, 33, 34] and (ii) provides consistent NN and many-body interactions, i.e., the same processes between different particles are described by the same LECs and operators. Order by order, predictions become more accurate and precise by a factor of $2 - 3$ at the cost of more involved calculations. Chiral EFT is valid for relative nucleon momenta below $\sim 500 - 600$ MeV [31], translating into densities below about twice the nuclear saturation density [22].

Solving the nuclear many-body problem is a challenging task that requires advanced computational tools. QMC methods are among the most precise nuclear many-body methods [12] and use stochastic techniques to extract ground-state properties of nuclear systems, providing exact solutions with only statistical uncertainties [19]. This is the main benefit over other computational methods whose additional approximations can lead to systematic uncertainties. However, QMC methods require local[1] interactions as input, i.e., interactions with no derivatives acting on the wave functions, to nonperturbatively solve the nuclear many-body problem. While chiral EFT is traditionally formulated in a nonlocal way and has been used to construct NN interactions to N^{3}LO and beyond [35, 36], local chiral EFT interactions have been introduced only in the past decade [13, 15, 17]. Local interactions have so far been developed up to N^{2}LO in chiral EFT [13] on the same footing as nonlocal interactions. In addition, maximally-local interactions with selected N^{3}LO contributions have been developed [15] but these typically do not include N^{3}LO pion-exchange contributions. Finally, recent work saw the development of local N^{3}LO interactions where all nonlocalities were neglected and replaced by local operators where possible, even when the latter are connected by FRF [17].

[1] Note that small nonlocalities can be treated perturbatively.

Here, we develop, for the first time, *complete* maximally-local NN interactions at N^{3}LO in chiral EFT that are suited for QMC calculations, i.e., interactions that account for all short- and long-range contributions and all necessary local and nonlocal pieces up to that order, using FRF. While FRF is violated when local regulators are applied [17, 18], this effect induces regulator artifacts that take the form of interaction pieces of higher order in the EFT expansion, and hence, decrease in size. We have shown that the most sizable regulator artifacts at LO can be absorbed by the regular interactions pieces at NLO [18]. Similarly, artifacts at NLO and subleading artifacts at LO can be absorbed at N^{3}LO. Hence, the remaining artifacts are of order $(Q/\Lambda_c)^6$, and can be expected to be small. Furthermore, we study interactions at large cutoffs where these regulator artifacts further decrease in size. For these reasons, regulator artifacts in the NN sector are small in this work.

B. Maximally-Local Hamiltonian at N^{3}LO

The chiral EFT Hamiltonian is given in terms of a momentum expansion and can be decomposed into short-range contact pieces and long-range pieces mediated by one and multiple pion exchanges,

$$V^{(\nu)} = V^{(\nu)}_{\rm cont} + V^{(\nu)}_{\pi}, \tag{1}$$

where ν is the chiral order, indicating the power $(Q/\Lambda_b)^\nu$.

1. *Contact interactions*

Up to N^{2}LO, the contact interactions can be fully expressed using only local operators and the nonlocal spin-orbit interaction that can be treated by QMC methods [13, 14, 21, 37]. The leading-order (LO) momentum-independent contact interactions are given by

$$V^{(0)}_{\rm cont} = C_S + C_T \boldsymbol{\sigma}_1 \cdot \boldsymbol{\sigma}_2 \,, \tag{2}$$

where two out of four possible operators are chosen [14, 18][2]. The remaining two operators are linearly dependent due to the required antisymmetry of the wave function in nuclear systems. Any two out of these four operators, describing both NN S-wave interaction channels, can be selected using FRF [18].

At NLO, the contact interaction is momentum dependent. For initial and final nucleon momenta $\mathbf{p}$ and $\mathbf{p}'$, momentum transfer $\mathbf{q} = \mathbf{p}' - \mathbf{p}$, and momentum transfer in the exchange channel $\mathbf{k} = (\mathbf{p}' + \mathbf{p})/2$, the NLO interaction is given by

$$\begin{aligned} V^{(2)}_{\rm cont} = \;& C_1 \boldsymbol{q}^2 + C_2 \boldsymbol{q}^2 \boldsymbol{\tau}_1 \cdot \boldsymbol{\tau}_2 + C_3 \boldsymbol{q}^2 \boldsymbol{\sigma}_1 \cdot \boldsymbol{\sigma}_2 \\ & + C_4 \boldsymbol{q}^2 \boldsymbol{\sigma}_1 \cdot \boldsymbol{\sigma}_2 \boldsymbol{\tau}_1 \cdot \boldsymbol{\tau}_2 + \frac{i}{2} C_5 \, (\boldsymbol{\sigma}_1 + \boldsymbol{\sigma}_2) \cdot (\boldsymbol{q} \times \boldsymbol{k}) \\ & + C_6 \, (\boldsymbol{\sigma}_1 \cdot \boldsymbol{q}) \, (\boldsymbol{\sigma}_2 \cdot \boldsymbol{q}) + C_7 \, (\boldsymbol{\sigma}_1 \cdot \boldsymbol{q}) \, (\boldsymbol{\sigma}_2 \cdot \boldsymbol{q}) \boldsymbol{\tau}_1 \cdot \boldsymbol{\tau}_2, \end{aligned} \tag{3}$$

where, again, a subset of 7 out of 14 operators has been chosen. At NLO, the operators are selected such that the interaction is fully local except for the spin-orbit interaction. Other choices are possible, too, which lead to nonlocal or partially local interactions [35, 36, 38–40]. There are no new contact operators that appear at N^{2}LO.

We now turn to N^{3}LO where there are total of 30 possible contact operators [39],

$$\begin{aligned} V^{(4)}_{\rm cont} = \;& \alpha_1 \boldsymbol{q}^4 + \alpha_2 \boldsymbol{q}^4 \boldsymbol{\tau}_1 \cdot \boldsymbol{\tau}_2 + \alpha_3 \boldsymbol{q}^4 \boldsymbol{\sigma}_1 \cdot \boldsymbol{\sigma}_2 + \alpha_4 \boldsymbol{q}^4 \boldsymbol{\sigma}_1 \cdot \boldsymbol{\sigma}_2 \boldsymbol{\tau}_1 \cdot \boldsymbol{\tau}_2 \\ & + \alpha_5 \boldsymbol{k}^4 + \alpha_6 \boldsymbol{k}^4 \boldsymbol{\tau}_1 \cdot \boldsymbol{\tau}_2 + \alpha_7 \boldsymbol{k}^4 \boldsymbol{\sigma}_1 \cdot \boldsymbol{\sigma}_2 + \alpha_8 \boldsymbol{k}^4 \boldsymbol{\sigma}_1 \cdot \boldsymbol{\sigma}_2 \boldsymbol{\tau}_1 \cdot \boldsymbol{\tau}_2 \\ & + \alpha_9 \boldsymbol{q}^2 \boldsymbol{k}^2 + \alpha_{10} \boldsymbol{q}^2 \boldsymbol{k}^2 \boldsymbol{\tau}_1 \cdot \boldsymbol{\tau}_2 + \alpha_{11} \boldsymbol{q}^2 \boldsymbol{k}^2 \boldsymbol{\sigma}_1 \cdot \boldsymbol{\sigma}_2 + \alpha_{12} \boldsymbol{q}^2 \boldsymbol{k}^2 \boldsymbol{\sigma}_1 \cdot \boldsymbol{\sigma}_2 \boldsymbol{\tau}_1 \cdot \boldsymbol{\tau}_2 \\ & + \alpha_{13} \, (\boldsymbol{q} \times \boldsymbol{k})^2 + \alpha_{14} \, (\boldsymbol{q} \times \boldsymbol{k})^2 \boldsymbol{\tau}_1 \cdot \boldsymbol{\tau}_2 + \alpha_{15} \, (\boldsymbol{q} \times \boldsymbol{k})^2 \boldsymbol{\sigma}_1 \cdot \boldsymbol{\sigma}_2 + \alpha_{16} \, (\boldsymbol{q} \times \boldsymbol{k})^2 \boldsymbol{\sigma}_1 \cdot \boldsymbol{\sigma}_2 \boldsymbol{\tau}_1 \cdot \boldsymbol{\tau}_2 \\ & + \frac{i}{2} \alpha_{17} \boldsymbol{q}^2 (\boldsymbol{\sigma}_1 + \boldsymbol{\sigma}_2) \cdot (\boldsymbol{q} \times \boldsymbol{k}) + \frac{i}{2} \alpha_{18} \boldsymbol{q}^2 (\boldsymbol{\sigma}_1 + \boldsymbol{\sigma}_2) \cdot (\boldsymbol{q} \times \boldsymbol{k}) \boldsymbol{\tau}_1 \cdot \boldsymbol{\tau}_2 \\ & + \frac{i}{2} \alpha_{19} \boldsymbol{k}^2 (\boldsymbol{\sigma}_1 + \boldsymbol{\sigma}_2) \cdot (\boldsymbol{q} \times \boldsymbol{k}) + \frac{i}{2} \alpha_{20} \boldsymbol{k}^2 (\boldsymbol{\sigma}_1 + \boldsymbol{\sigma}_2) \cdot (\boldsymbol{q} \times \boldsymbol{k}) \boldsymbol{\tau}_1 \cdot \boldsymbol{\tau}_2 \\ & + \alpha_{21} \boldsymbol{q}^2 \, \boldsymbol{\sigma}_1 \cdot \boldsymbol{q} \, \boldsymbol{\sigma}_2 \cdot \boldsymbol{q} + \alpha_{22} \boldsymbol{q}^2 \, \boldsymbol{\sigma}_1 \cdot \boldsymbol{q} \, \boldsymbol{\sigma}_2 \cdot \boldsymbol{q} \, \boldsymbol{\tau}_1 \cdot \boldsymbol{\tau}_2 + \alpha_{23} \boldsymbol{k}^2 \, \boldsymbol{\sigma}_1 \cdot \boldsymbol{q} \, \boldsymbol{\sigma}_2 \cdot \boldsymbol{q} + \alpha_{24} \boldsymbol{k}^2 \, \boldsymbol{\sigma}_1 \cdot \boldsymbol{q} \, \boldsymbol{\sigma}_2 \cdot \boldsymbol{q} \, \boldsymbol{\tau}_1 \cdot \boldsymbol{\tau}_2 \\ & + \alpha_{25} \boldsymbol{q}^2 \, \boldsymbol{\sigma}_1 \cdot \boldsymbol{k} \, \boldsymbol{\sigma}_2 \cdot \boldsymbol{k} + \alpha_{26} \boldsymbol{q}^2 \, \boldsymbol{\sigma}_1 \cdot \boldsymbol{k} \, \boldsymbol{\sigma}_2 \cdot \boldsymbol{k} \, \boldsymbol{\tau}_1 \cdot \boldsymbol{\tau}_2 + \alpha_{27} \boldsymbol{k}^2 \, \boldsymbol{\sigma}_1 \cdot \boldsymbol{k} \, \boldsymbol{\sigma}_2 \cdot \boldsymbol{k} + \alpha_{28} \boldsymbol{k}^2 \, \boldsymbol{\sigma}_1 \cdot \boldsymbol{k} \, \boldsymbol{\sigma}_2 \cdot \boldsymbol{k} \, \boldsymbol{\tau}_1 \cdot \boldsymbol{\tau}_2 \\ & + \alpha_{29} \, \boldsymbol{\sigma}_1 \cdot (\boldsymbol{q} \times \boldsymbol{k}) \, \boldsymbol{\sigma}_2 \cdot (\boldsymbol{q} \times \boldsymbol{k}) + \alpha_{30} \, \boldsymbol{\sigma}_1 \cdot (\boldsymbol{q} \times \boldsymbol{k}) \, \boldsymbol{\sigma}_2 \cdot (\boldsymbol{q} \times \boldsymbol{k}) \boldsymbol{\tau}_1 \cdot \boldsymbol{\tau}_2 \,. \end{aligned} \tag{4}$$

[2] In this case, isospin-dependent operators are neglected.

Note, that terms $\sim (\boldsymbol{q}\cdot\boldsymbol{k})^2$ can be expressed in terms of $\boldsymbol{q}^2\boldsymbol{k}^2$ and $(\boldsymbol{q}\times\boldsymbol{k})^2$, and hence, do not have to be included explicitly. Also, the last two operators are related to a squared spin-orbit operator and the angular momentum operator by

$$\frac{1}{2}\left((\boldsymbol{\sigma}_1+\boldsymbol{\sigma}_2)\cdot(\boldsymbol{q}\times\boldsymbol{k})\right)^2 = \boldsymbol{\sigma}_1\cdot(\boldsymbol{q}\times\boldsymbol{k})\,\boldsymbol{\sigma}_2\cdot(\boldsymbol{q}\times\boldsymbol{k}) + (\boldsymbol{q}\times\boldsymbol{k})^2\,. \quad (5)$$

Due to FRF, we can again choose a subset of 15 operators from this complete set. When selecting the subset, however, it is crucial to choose operators in such a way that upon antisymmetrization the complete operator set is recovered. Hence, for example, a nonlocal tensor operator cannot be replaced by a central local interaction piece as physics-information at that order would be lost. Here, we choose the following subset of operators:

$$\begin{aligned} V_{\rm cont}^{(4)} = \;& D_1\,\boldsymbol{q}^4 + D_2\,\boldsymbol{q}^4\boldsymbol{\tau}_1\cdot\boldsymbol{\tau}_2 + D_3\,\boldsymbol{q}^4\boldsymbol{\sigma}_1\cdot\boldsymbol{\sigma}_2 \\ & + D_4\,\boldsymbol{q}^4\boldsymbol{\sigma}_1\cdot\boldsymbol{\sigma}_2\boldsymbol{\tau}_1\cdot\boldsymbol{\tau}_2 + \frac{i}{2}D_5\,\boldsymbol{q}^2(\boldsymbol{\sigma}_1+\boldsymbol{\sigma}_2)\cdot(\boldsymbol{q}\times\boldsymbol{k}) \\ & + \frac{i}{2}D_6\,\boldsymbol{q}^2(\boldsymbol{\sigma}_1+\boldsymbol{\sigma}_2)\cdot(\boldsymbol{q}\times\boldsymbol{k})\boldsymbol{\tau}_1\cdot\boldsymbol{\tau}_2 \\ & + D_7\,\boldsymbol{q}^2\,\boldsymbol{\sigma}_1\cdot\boldsymbol{q}\,\boldsymbol{\sigma}_2\cdot\boldsymbol{q} + D_8\,\boldsymbol{q}^2\,\boldsymbol{\sigma}_1\cdot\boldsymbol{q}\,\boldsymbol{\sigma}_2\cdot\boldsymbol{q}\,\boldsymbol{\tau}_1\cdot\boldsymbol{\tau}_2 \\ & + D_9\,\boldsymbol{q}^2\boldsymbol{k}^2 + D_{10}\,\boldsymbol{q}^2\boldsymbol{k}^2\boldsymbol{\tau}_1\cdot\boldsymbol{\tau}_2 + D_{11}\,(\boldsymbol{q}\times\boldsymbol{k})^2 \\ & + D_{12}\,(\boldsymbol{q}\times\boldsymbol{k})^2\boldsymbol{\tau}_1\cdot\boldsymbol{\tau}_2 + D_{13}\,\boldsymbol{k}^2\,\boldsymbol{\sigma}_1\cdot\boldsymbol{q}\,\boldsymbol{\sigma}_2\cdot\boldsymbol{q} \\ & + D_{14}\,\boldsymbol{k}^2\,\boldsymbol{\sigma}_1\cdot\boldsymbol{q}\,\boldsymbol{\sigma}_2\cdot\boldsymbol{q}\,\boldsymbol{\tau}_1\cdot\boldsymbol{\tau}_2 \\ & + D_{15}\,\boldsymbol{\sigma}_1\cdot(\boldsymbol{q}\times\boldsymbol{k})\,\boldsymbol{\sigma}_2\cdot(\boldsymbol{q}\times\boldsymbol{k})\,. \end{aligned} \quad (6)$$

Note that operators D_1 to D_8 are local and D_9 to D_{15} are nonlocal. The coordinate space expressions of the local operators are given in Appendix A.

We can further reduce the number of nonlocal contacts as it has been found that there are redundancies among the 15 contact operators at N^{3}LO [36, 41]. By performing a unitary transformation (UT) on the Hamiltonian, we can decrease the number of independent nonlocal contacts to 4 [36]. Following Ref. [36], we consider the following unitary operator,

$$U = e^{\gamma_1 T_1+\gamma_2 T_2+\gamma_3 T_3}\,, \quad (7)$$

where T_i are the 3 antihermitian generators of the UT and γ_i are the corresponding transformation angles. Similarly to Ref. [36], we choose the following generators:

$$T_1 = \frac{m_N}{2\Lambda_b^4}\boldsymbol{k}\cdot\boldsymbol{q}\,, \quad (8)$$

$$T_2 = \frac{m_N}{2\Lambda_b^4}\boldsymbol{k}\cdot\boldsymbol{q}\;\boldsymbol{\tau}_1\cdot\boldsymbol{\tau}_2\,, \quad (9)$$

$$T_3 = \frac{m_N}{2\Lambda_b^4}(\boldsymbol{\sigma}_1\cdot\boldsymbol{k}\boldsymbol{\sigma}_2\cdot\boldsymbol{q}+\boldsymbol{\sigma}_1\cdot\boldsymbol{q}\boldsymbol{\sigma}_2\cdot\boldsymbol{k})\;\boldsymbol{\tau}_1\cdot\boldsymbol{\tau}_2\,. \quad (10)$$

Note that Eqs. (8), (9) and (10) constitute one choice of basis for the UT and other choices are possible due to FRF. For example, Ref. [36] replaces the operator $\boldsymbol{\tau}_1\cdot\boldsymbol{\tau}_2$ by $\boldsymbol{\sigma}_1\cdot\boldsymbol{\sigma}_2$ in Eq. (9) and, $\boldsymbol{\tau}_1\cdot\boldsymbol{\tau}_2$ with I in Eq. (10). We need to apply the UT only to the LO Hamiltonian since the UT, when applied to the higher-order interactions, will induce terms at order Q^5 and above which is beyond the desired accuracy for this work. The shift in the LO Hamiltonian is given by

$$\begin{aligned} \delta H^0 &= U^\dagger H^0 U - H^0 \\ &= \sum_i \gamma_i [H^0, T_i] + \ldots \\ &= \sum_i \gamma_i [(H^{\rm kin} + V_{1\pi}^{(0)} + V_{\rm cont}^{(0)}), T_i] + \ldots\,, \end{aligned} \quad (11)$$

where the dots represent terms above the accuracy of our calculation. It can be shown that $[V_{1\pi}^{(0)}, T_i]$ and $[V_{\rm cont}^{(0)}, T_i]$ only induce shifts to contact operators of order Q^0 and Q^2 and therefore do not need to be considered explicitly [36]. On the other hand, the commutator with the kinetic energy generates order Q^4 terms, see Ref. [36]:

$$\begin{aligned} \sum_i \gamma_i [H^{\rm kin}, T_i] = \;& \frac{\gamma_1}{\Lambda_b^4}(\boldsymbol{k}\cdot\boldsymbol{q})^2 + \frac{\gamma_2}{\Lambda_b^4}(\boldsymbol{k}\cdot\boldsymbol{q})^2\boldsymbol{\tau}_1\cdot\boldsymbol{\tau}_2 \\ & + \frac{\gamma_3}{\Lambda_b^4}(\boldsymbol{k}\cdot\boldsymbol{q})(\boldsymbol{\sigma}_1\cdot\boldsymbol{k}\boldsymbol{\sigma}_2\cdot\boldsymbol{q}+\boldsymbol{\sigma}_1\cdot\boldsymbol{q}\boldsymbol{\sigma}_2\cdot\boldsymbol{k})\boldsymbol{\tau}_1\cdot\boldsymbol{\tau}_2\,. \end{aligned} \quad (12)$$

Using the identity

$$(\boldsymbol{k}\cdot\boldsymbol{q})^2 = \boldsymbol{q}^2\boldsymbol{k}^2 - (\boldsymbol{q}\times\boldsymbol{k})^2\,, \quad (13)$$

and Eq. (10) of Ref. [36],

$$\begin{aligned} (\boldsymbol{k}\cdot\boldsymbol{q})(\boldsymbol{\sigma}_1\cdot\boldsymbol{k}\boldsymbol{\sigma}_2\cdot\boldsymbol{q}+\boldsymbol{\sigma}_1\cdot\boldsymbol{q}\boldsymbol{\sigma}_2\cdot\boldsymbol{k}) = & -(\boldsymbol{q}\times\boldsymbol{k})^2\boldsymbol{\sigma}_1\cdot\boldsymbol{\sigma}_2 \\ & + \boldsymbol{q}^2\boldsymbol{\sigma}_1\cdot\boldsymbol{k}\boldsymbol{\sigma}_2\cdot\boldsymbol{k} \\ & + \boldsymbol{k}^2\boldsymbol{\sigma}_1\cdot\boldsymbol{q}\boldsymbol{\sigma}_2\cdot\boldsymbol{q} \\ & + \boldsymbol{\sigma}_1\cdot(\boldsymbol{q}\times\boldsymbol{k})\,\boldsymbol{\sigma}_2\cdot(\boldsymbol{q}\times\boldsymbol{k})\,, \end{aligned} \quad (14)$$

we can express Eqs. (11) and (12) as

$$\begin{aligned} \delta H^0 = \;& \frac{\gamma_1}{\Lambda_b^4}\boldsymbol{q}^2\boldsymbol{k}^2 + \frac{\gamma_2}{\Lambda_b^4}\boldsymbol{q}^2\boldsymbol{k}^2\boldsymbol{\tau}_1\cdot\boldsymbol{\tau}_2 \\ & - \frac{\gamma_1}{\Lambda_b^4}(\boldsymbol{q}\times\boldsymbol{k})^2 - \frac{\gamma_2}{\Lambda_b^4}(\boldsymbol{q}\times\boldsymbol{k})^2\boldsymbol{\tau}_1\cdot\boldsymbol{\tau}_2 \\ & - \frac{\gamma_3}{\Lambda_b^4}(\boldsymbol{q}\times\boldsymbol{k})^2\boldsymbol{\sigma}_1\cdot\boldsymbol{\sigma}_2\boldsymbol{\tau}_1\cdot\boldsymbol{\tau}_2 \\ & + \frac{\gamma_3}{\Lambda_b^4}\boldsymbol{q}^2\boldsymbol{\sigma}_1\cdot\boldsymbol{k}\boldsymbol{\sigma}_2\cdot\boldsymbol{k}\boldsymbol{\tau}_1\cdot\boldsymbol{\tau}_2 \\ & + \frac{\gamma_3}{\Lambda_b^4}\boldsymbol{k}^2\boldsymbol{\sigma}_1\cdot\boldsymbol{q}\boldsymbol{\sigma}_2\cdot\boldsymbol{q}\boldsymbol{\tau}_1\cdot\boldsymbol{\tau}_2 \\ & + \frac{\gamma_3}{\Lambda_b^4}\boldsymbol{\sigma}_1\cdot(\boldsymbol{q}\times\boldsymbol{k})\,\boldsymbol{\sigma}_2\cdot(\boldsymbol{q}\times\boldsymbol{k})\boldsymbol{\tau}_1\cdot\boldsymbol{\tau}_2\,. \end{aligned} \quad (15)$$

Note that some of the new operators,

$$\begin{aligned} \{&(\boldsymbol{q}\times\boldsymbol{k})^2\boldsymbol{\sigma}_1\cdot\boldsymbol{\sigma}_2\boldsymbol{\tau}_1\cdot\boldsymbol{\tau}_2, \boldsymbol{q}^2\boldsymbol{\sigma}_1\cdot\boldsymbol{k}\boldsymbol{\sigma}_2\cdot\boldsymbol{k}\boldsymbol{\tau}_1\cdot\boldsymbol{\tau}_2, \\ & \boldsymbol{\sigma}_1\cdot(\boldsymbol{q}\times\boldsymbol{k})\,\boldsymbol{\sigma}_2\cdot(\boldsymbol{q}\times\boldsymbol{k})\boldsymbol{\tau}_1\cdot\boldsymbol{\tau}_2\}\,, \end{aligned} \quad (16)$$

are not explicitly chosen in Eq. (6), but they are linearly dependent operators, see Eq. (4). Therefore, we do not need to consider them explicitly any further.

Having carried out the UT and including the shift to the Hamiltonian, the N^{3}LO contact interaction is now

$$\begin{aligned} V_{\rm cont}^{(4)} = \quad & D_1\,\boldsymbol{q}^4 + D_2\,\boldsymbol{q}^4\boldsymbol{\tau}_1\cdot\boldsymbol{\tau}_2 + D_3\,\boldsymbol{q}^4\boldsymbol{\sigma}_1\cdot\boldsymbol{\sigma}_2 \\ & + D_4\,\boldsymbol{q}^4\boldsymbol{\sigma}_1\cdot\boldsymbol{\sigma}_2\boldsymbol{\tau}_1\cdot\boldsymbol{\tau}_2 + \frac{i}{2}D_5\,\boldsymbol{q}^2(\boldsymbol{\sigma}_1+\boldsymbol{\sigma}_2)\cdot(\boldsymbol{q}\times\boldsymbol{k}) \\ & + \frac{i}{2}D_6\,\boldsymbol{q}^2(\boldsymbol{\sigma}_1+\boldsymbol{\sigma}_2)\cdot(\boldsymbol{q}\times\boldsymbol{k})\boldsymbol{\tau}_1\cdot\boldsymbol{\tau}_2 \\ & + D_7\,\boldsymbol{q}^2\,\boldsymbol{\sigma}_1\cdot\boldsymbol{q}\,\boldsymbol{\sigma}_2\cdot\boldsymbol{q} + D_8\,\boldsymbol{q}^2\,\boldsymbol{\sigma}_1\cdot\boldsymbol{q}\,\boldsymbol{\sigma}_2\cdot\boldsymbol{q}\,\boldsymbol{\tau}_1\cdot\boldsymbol{\tau}_2 \\ & + \left(D_9+\frac{\gamma_1}{\Lambda_b^4}\right)\boldsymbol{q}^2\boldsymbol{k}^2 + \left(D_{10}+\frac{\gamma_2}{\Lambda_b^4}\right)\boldsymbol{q}^2\boldsymbol{k}^2\boldsymbol{\tau}_1\cdot\boldsymbol{\tau}_2 \\ & + \left(D_{11}-\frac{\gamma_1}{\Lambda_b^4}\right)(\boldsymbol{q}\times\boldsymbol{k})^2 \\ & + \left(D_{12}-\frac{\gamma_2}{\Lambda_b^4}\right)(\boldsymbol{q}\times\boldsymbol{k})^2\boldsymbol{\tau}_1\cdot\boldsymbol{\tau}_2 \\ & + D_{13}\,\boldsymbol{k}^2\,\boldsymbol{\sigma}_1\cdot\boldsymbol{q}\,\boldsymbol{\sigma}_2\cdot\boldsymbol{q} \\ & + \left(D_{14}+\frac{\gamma_3}{\Lambda_b^4}\right)\boldsymbol{k}^2\,\boldsymbol{\sigma}_1\cdot\boldsymbol{q}\,\boldsymbol{\sigma}_2\cdot\boldsymbol{q}\,\boldsymbol{\tau}_1\cdot\boldsymbol{\tau}_2 \\ & + D_{15}\,\boldsymbol{\sigma}_1\cdot(\boldsymbol{q}\times\boldsymbol{k})\,\boldsymbol{\sigma}_2\cdot(\boldsymbol{q}\times\boldsymbol{k})\,. \end{aligned} \tag{17}$$

The variables γ_1, γ_2 and γ_3 are completely arbitrary parameters of the UT and can be chosen to remove nonlocal operators. The parameter γ_1 can be chosen to be either $-\Lambda_b^4 D_9$ or $\Lambda_b^4 D_{11}$, removing either of the two corresponding contact operators. Similarly, γ_2 can be chosen as either $-\Lambda_b^4 D_{10}$ or $\Lambda_b^4 D_{12}$. Finally, γ_3 can be set to $-\Lambda_b^4 D_{14}$[3]. Therefore, we see that using the UT we can remove all but 4 nonlocal operators.

In this paper, we set $\gamma_1 = -\Lambda_b^4 D_9$, $\gamma_2 = -\Lambda_b^4 D_{10}$ and $\gamma_3 = -\Lambda_b^4 D_{14}$. The nonlocal part of the N^{3}LO contact interaction then consists of only 4 operators:

$$\begin{aligned} V_{\rm cont,nonlocal}^{(4)} = & \tilde{D}_{11}\,\boldsymbol{L}^2 + \tilde{D}_{12}\,\boldsymbol{L}^2\boldsymbol{\tau}_1\cdot\boldsymbol{\tau}_2 \\ & + \tilde{D}_{13}\,\boldsymbol{k}^2\,\boldsymbol{\sigma}_1\cdot\boldsymbol{q}\,\boldsymbol{\sigma}_2\cdot\boldsymbol{q} \\ & + \tilde{D}_{15}\,(\boldsymbol{\sigma}_1\cdot\boldsymbol{L})(\boldsymbol{\sigma}_2\cdot\boldsymbol{L})\,, \end{aligned} \tag{18}$$

where we have used the total orbital angular momentum operator $\boldsymbol{L} = (\boldsymbol{q}\times\boldsymbol{k})$. We will refer to our maximally local N^{3}LO interactions with this choice of 4 nonlocal operators by N^{3}LO$_{\rm LA}$-09, N^{3}LO$_{\rm LA}$-08, N^{3}LO$_{\rm LA}$-07, and N^{3}LO$_{\rm LA}$-06, where the number refers to the cutoff in coordinate space. We have also considered other possible choices for the set of 4 nonlocal operators, see Appendix B, but found the set chosen in this work to be best suited for QMC methods because three operators can be directly mapped into the 18 operator channels of the phenomenological Argonne V18 (AV18) interaction [42] that has been used extensively in QMC simulations.

[3] In fact, due to the Fierz ambiguity, γ_3 can be used to remove also other nonlocal operators, see Eq. (16).

In summary, our N^{3}LO$_{\rm LA}$ interactions contain 21 contacts in total, out of which 4 are nonlocal. The corresponding 21 LECs are determined by fits to *np* phase shifts, see Sec. III for details.

2. *Pion-exchange interactions*

The long-range and intermediate-range parts of the nuclear interactions in chiral EFT are mediated by pion exchanges. All pion-exchange interactions to N^{3}LO are either fully local or accompanied by the spin-orbit operator, and thus, we directly give the coordinate space expressions here.

Without loss of generality, the pion-exchange part of the Hamiltonian can be decomposed as

$$\begin{aligned} V_\pi = \quad & V_C(r) + W_C(r)\boldsymbol{\tau}_1\cdot\boldsymbol{\tau}_2 \\ & + \left(V_S(r) + W_S(r)\boldsymbol{\tau}_1\cdot\boldsymbol{\tau}_2\right)\boldsymbol{\sigma}_1\cdot\boldsymbol{\sigma}_2 \\ & + \left(V_T(r) + W_T(r)\boldsymbol{\tau}_1\cdot\boldsymbol{\tau}_2\right)S_{12} \\ & + \left(V_{LS}(r) + W_{LS}(r)\boldsymbol{\tau}_1\cdot\boldsymbol{\tau}_2\right)\boldsymbol{L}\cdot\boldsymbol{S}\,, \end{aligned} \tag{19}$$

where $S_{12} = (3\boldsymbol{\sigma}_1\cdot\hat{\boldsymbol{r}}\,\boldsymbol{\sigma}_2\cdot\hat{\boldsymbol{r}} - \boldsymbol{\sigma}_1\cdot\boldsymbol{\sigma}_2)$ is the tensor operator and $\boldsymbol{S}$ is the total spin operator.

At LO, only the one-pion exchange (OPE) contributes to the Hamiltonian. It is given by [13, 14, 17],

$$\begin{aligned} W_S(r) = \quad & \frac{g_A^2 m_\pi^2}{48\pi f_\pi^2}\frac{e^{-x}}{r} \\ W_T(r) = \quad & \frac{g_A^2}{48\pi f_\pi^2}\frac{e^{-x}}{r^3}(3+3x+x^2), \end{aligned} \tag{20}$$

where $x = m_\pi r$, m_π is the pion mass, g_A is the axial-vector coupling constant, and f_π is the pion decay constant. Here, we use the charge-independence breaking form of the OPE as we have done before, see Ref. [14] for details.

At NLO and beyond, V_π receives contribution from two-pion exchange (TPE) diagrams. For these TPE pieces, we employ the expressions using spectral-function regularization (SFR) [13, 17, 39]. Under this representation, the TPE potential is written in terms of spectral functions as

$$\begin{aligned} V_C(r) = \quad & \frac{1}{2\pi^2 r}\int_{2m_\pi}^{\tilde{\Lambda}} d\mu\mu e^{-\mu r}{\rm Im}V_C(i\mu) \\ V_S(r) = \quad & -\frac{1}{6\pi^2 r}\int_{2m_\pi}^{\tilde{\Lambda}} d\mu\mu e^{-\mu r}[\mu^2{\rm Im}\,V_T(i\mu) \\ & \qquad - 3{\rm Im}\,V_S(i\mu)] \\ V_T(r) = \quad & -\frac{1}{6\pi^2 r^3}\int_{2m_\pi}^{\tilde{\Lambda}} d\mu\mu e^{-\mu r}(3+3\mu r+\mu^2 r^2) \\ & \qquad \times {\rm Im}\,V_T(i\mu) \\ V_{LS}(r) = \quad & \frac{1}{2\pi^2 r^3}\int_{2m_\pi}^{\tilde{\Lambda}} d\mu\mu e^{-\mu r}(1+\mu r){\rm Im}V_{LS}(i\mu), \end{aligned} \tag{21}$$

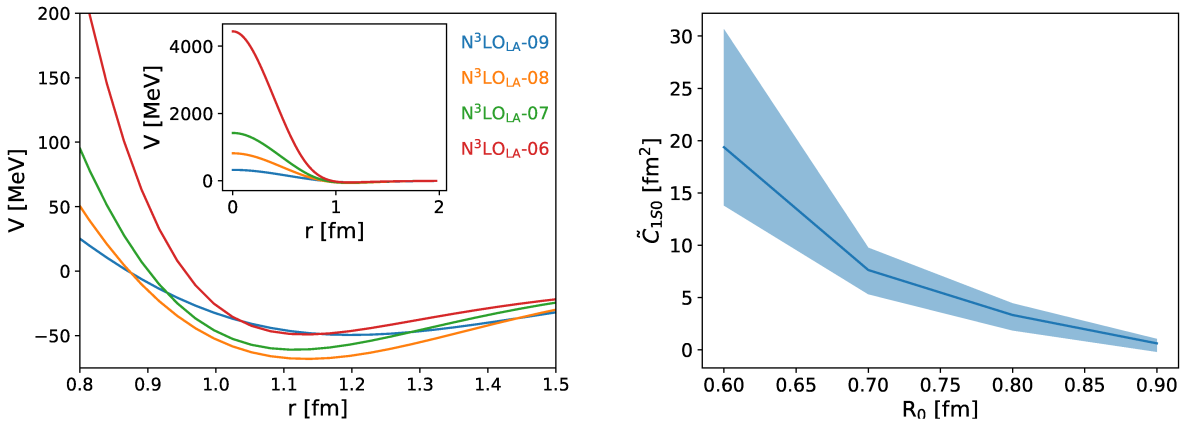

FIG. 1. (a) The local part of our N^3LO_{LA} interactions in the $^1S_0$ channel (i.e., 17 local contacts and all the pion-exchange pieces) for the least-squares fit as a function of particle separation r. The LECs are obtained via least-squares fits as described in Sec. III. We show the interactions for different cutoff values, i.e. N^3LO_{LA}-09 to N^3LO_{LA}-06. Panel (b) shows the cutoff dependence of the LO spectral LEC in the $^1S_0$ partial wave at N^3LO. The solid blue line shows the least-squares results whereas the band represents the 95% confidence level (CL) calculated using a Bayesian analysis, see Sec. III.

and similarly for $W_{C,S,T,LS}$. All TPE contributions to the Hamiltonian at NLO, N^2LO, and N^3LO can therefore be specified in terms of the spectral functions that appear in Eq. (21). The explicit expressions for these spectral functions can be found in Appendix A of Ref. [17]. We note that we add to $V_\pi^{(4)}$ the $1/M_N$ corrections to the N^2LO TPE potential. These corrections nominally appear at 5th order in chiral EFT but, as is common practice [17, 39], we include it at N^3LO in order to arrive at a more realistic intermediate-range attraction. Also, note that unlike Ref. [17], we do not take the limit $\tilde{\Lambda} \to \infty$ but leave the SFR cutoff finite. In this work, the SFR cutoff $\tilde{\Lambda}$ is fixed at the value of 1 GeV, similar to Refs. [13, 39].

The strength of the TPE potential is determined by the πN couplings which are strongly constrained by chiral symmetry and can be determined by analyses of low-energy πN-scattering. Here, we employ the values obtained from a Roy-Steiner (RS) analysis of πN scattering [43] at N^3LO. At N^2LO, we chose the same values as in Ref. [13, 14] for consistency with our previous interactions. These values are very close to the values extracted from the RS analysis except for c_4. The values of the couplings employed in this work are given in Table I.

πN coupling	N^2LO	N^3LO
$c_1[\mathrm{GeV}^{-1}]$	-0.81	-1.07
$c_2[\mathrm{GeV}^{-1}]$	–	3.20
$c_3[\mathrm{GeV}^{-1}]$	-3.4	-5.32
$c_4[\mathrm{GeV}^{-1}]$	3.4	3.56
$\bar{d}_1+\bar{d}_2[\mathrm{GeV}^{-2}]$	–	1.04
$\bar{d}_3[\mathrm{GeV}^{-2}]$	–	-0.48
$\bar{d}_5[\mathrm{GeV}^{-2}]$	–	0.14
$\bar{d}_{14}-\bar{d}_{15}[\mathrm{GeV}^{-2}]$	–	-1.90

TABLE I. The πN couplings used in this work. The couplings at N^2LO are taken from Ref. [13, 14] whereas the couplings at N^3LO are taken from Ref. [43].

C. Regulators

The chiral EFT interactions developed here need to be regulated at short distances/high momenta to be employed in many-body computational methods:

$$V_{\rm cont}^{(\nu)} \longrightarrow V_{\rm cont}^{(\nu)} \times f_{\rm short}(r)\,, \qquad V_\pi^{(\nu)} \longrightarrow V_\pi^{(\nu)} \times f_{\rm long}(r)\,. \tag{22}$$

To define maximally-local Hamiltonians, we choose regulators that are fully local. We choose Gaussian regulators in position space, that can be expressed as

$$f_{\rm short}(r) = \frac{n}{4\pi R_0^3 \Gamma(3/n)} \exp\left(-\left(\frac{r}{R_0}\right)^n\right)\,, \tag{23}$$

$$f_{\rm long}(r) = \left(1-\exp\left(-\left(\frac{r}{R_0}\right)^{n_1}\right)\right)^{n_2}\,, \tag{24}$$

with $n = n_1 = 2$, $n_2 = 6$. We therefore, have one position-space cutoff parameter R_0 that regulates both the short- and long-range pieces of the interaction. Upon Fourier transformation (FT) of the regulator functions, the position-space cutoff can be related to the momentum-space cutoff Λ_c as $R_0 = 2/\Lambda_c$. In this paper, we study four different cutoffs, $R_0 = 0.9$ fm, 0.8 fm, 0.7 fm, and 0.6 fm, leading to four different interactions, N^3LO_{LA}-09 to N^3LO_{LA}-06.

III. ANALYSIS OF NN SCATTERING

In this work, the 21 operator LECs are determined by fits to *np* phase shifts, while in the future we will explore fits directly to scattering data. We perform the fits directly in momentum space using the formalism developed in Ref. [45]. This allows us to fit interactions that include nonlocal pieces, which is crucial at N^{3}LO. We take the phase-shift values from the Nijmegen partial-wave analysis (NPWA) [44], and incorporate EFT truncation uncertainties by performing Bayesian fits to these data. Bayes' theorem defines the posterior P as

$$P = \frac{\mathcal{L} \times \Pi}{Z}\,, \tag{25}$$

where Π is the prior distribution on the LECs, $\mathcal{L}$ is the Likelihood function that incorporates information from the phase shifts, and the evidence Z can, in principle, be used to perform model comparison. However, in this work we treat Z as a normalization constant for a given set of model assumptions. We take the prior Π to be uniform everywhere in parameter space, because the LECs size can vary strongly as we vary the cutoff. Furthermore, we employ a Gaussian model for the Likelihood function,

$$\mathcal{L} \propto \prod_i \exp\left\{ -\frac{1}{2}\left(\frac{X_i^{\rm exp} - X_i^{\rm theo}}{\sigma_i}\right)^2 \right\}, \tag{26}$$

where the product over i indicates a product over all considered partial waves and kinematic variables (lab energies). The variable X denotes an observable which, in this case, is the phase shift for a given lab energy and partial wave. The uncertainty σ_i receives two contributions,

$$\sigma_i^2 = \sigma_{\rm i,exp}^2 + \sigma_{\rm i,theo}^2\,, \tag{27}$$

where $\sigma_{\rm i,exp}$ are taken to be the uncertainties provided by the NPWA [44] and the $\sigma_{\rm i,theo}$ represent theoretical uncertainties. In this work, we model these uncertainties as the EFT truncation uncertainty, since other sources of theoretical uncertainties are subdominant [33]. We assume that the truncation uncertainty can be well represented by the prescription of Epelbaum et al. [33] (EKM), which was shown in Ref. [46] to give very similar uncertainty estimates in matter when compared with the more involved Gaussian process algorithms for uncertainty estimation [31, 34]. The EKM truncation uncertainty for the observable X at N^{3}LO is given as

$$\Delta X_{\rm EKM}^{\rm N^3LO} = \max\Bigg(Q^5 \left|X^{\rm LO}\right|, Q^3 \left|X^{\rm LO} - X^{\rm NLO}\right|, \\ Q^2 \left|X^{\rm NLO} - X^{\rm N^2LO}\right|, Q \left|X^{\rm N^2LO} - X^{\rm N^3LO}\right| \Bigg)\,, \tag{28}$$

where $Q \equiv \frac{\max(m_\pi, p)}{\min(\Lambda_b, \Lambda_c)}$. Here, p is a typical momentum of the system under study in the center of mass frame, Λ_b is the breakdown scale which we take to be 600 MeV [34], and Λ_c is the momentum-space cutoff. Expressions similar to Eq. (28) hold at all orders. In this work, we take $\sigma_{\rm i,theo} = \Delta X_{i,\rm EKM}$ for all partial waves.

For the fits at N^{2}LO and N^{3}LO, we set $X^{\rm LO} = 0$ because we have otherwise found very poor Bayesian fits at high lab energies, with many samples including resonances or spurious bound states. The reason for this is that, due to the large differences between the data and the LO predictions at high lab energies, the EKM uncertainty estimates are dominated by the poor LO predictions and are very large, removing the constraining power of any high-energy data points and leading to spurious structures. Hence, we treat the LO contribution as an outlier in the expansion, see also Ref. [47] for a similar treatment of the LO predictions.

Evaluating the EKM uncertainty, Eq. (28), at a given order requires knowledge of the phase shifts at all lower orders. Therefore, as an initial step to performing Bayesian fits, we first determine the LECs via a least-squares minimization of the objective function

$$\chi^2 = \frac{1}{m}\sum_i \left(\frac{X_i^{\rm exp} - X_i^{\rm theo}}{\sigma_{i,\rm exp}}\right)^2, \tag{29}$$

where m is the number of experimental data points included in the fit. At LO, the least-squares optimizations are done by fitting to the ^{1}S$_0$ and ^{3}S$_1$ partial waves up to a lab energy of $E_{\rm max} = 50$ MeV. At NLO and N^{2}LO, we fit the ^{1}S$_0$, ^{3}S$_1$, ϵ_1, ^{1}P$_1$, ^{3}P$_0$, ^{3}P$_1$, and ^{3}P$_2$ partial waves up to $E_{\rm max} = 150$ MeV. For these orders, we fit to phase shift values at energies specified in Ref. [14]. At N^{3}LO, we additionally include ^{3}D$_1$, ϵ_2, ^{1}D$_2$, ^{3}D$_2$, and ^{3}D$_3$ in the fit and we fit up to $E_{\rm max} = 250$ MeV, additionally including points at 200 MeV and 250 MeV [4]. The results of these fits serve as an order-by-order estimate of the EFT convergence that is used to estimate the EKM uncertainty (28) which, in turn, is used as an input for our Bayesian fits. Note that the χ^2 function used in the least-squares fit does not incorporate theoretical EFT truncation uncertainties. Therefore, the least-squares fits also serve as complementary analyses to the Bayesian fits and can be used to estimate the importance of modeling EFT truncation uncertainties when chiral EFT interactions are calibrated to scattering phase shifts.

In Fig. 1, Panel (a) shows the local component of our N^{3}LO interactions in the ^{1}S$_0$ channel, with the LECs determined via the above mentioned least-squares fits. The interaction becomes increasingly hard for smaller R_0 because the LO ^{1}S$_0$ spectral LEC $\tilde{C}_{1S0}$ increases rapidly with decreasing R_0, see panel (b) of Fig. 1.

[4] For the least-squares fit at $R_0 = 0.7$ fm alone, we chose $E_{\rm max} = 350$ MeV in order to remove a spurious resonance in the ^{1}P$_1$ channel at $E \sim 350$ MeV. We verified that this change of $E_{\rm max}$ has a negligible effect on the phase shifts below 350 MeV in all other channels.

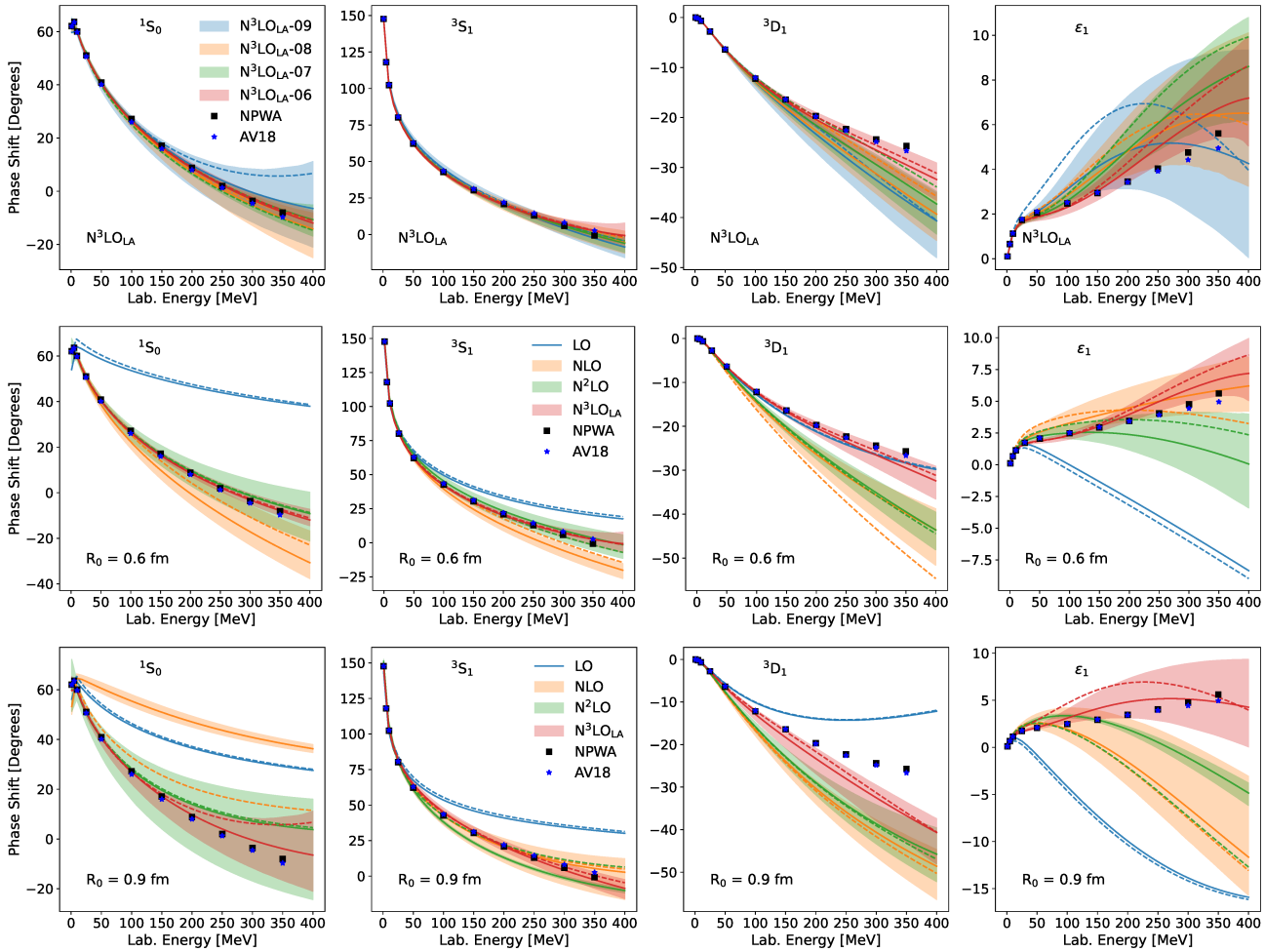

FIG. 2. Phase shifts in the $^1S_0$ and $^3S_1$-$^3D_1$ partial waves. In the top row, the chiral EFT order is fixed to be N^{3}LO and we show results for different cutoffs as indicated in the legend. In the middle (bottom) row, we show results for different chiral EFT orders at $R_0 = 0.6$ fm ($R_0 = 0.9$ fm). The bands correspond to the 95% CL. The solid lines represent the solutions that maximize the Bayesian posterior distributions while the dashed lines represent the least-squares fit results. For comparison, we show the Nijmegen partial-wave analysis [44] (black squares) and the AV18 phase shifts [42] (blue stars).

This growth is required to counter the attractive pion-exchange potential that becomes increasingly singular for lower coordinate-space cutoffs.

The Bayesian analyses are carried out by a Markov-Chain-Monte-Carlo (MCMC) sampling of the posterior distribution defined in Eq. (25). The details of the Bayesian fits, i.e. the partial waves involved and $E_{\rm max}$ at a given order, are the same as in the least-squares fit. The MCMC sampling results in a large number of samples drawn from the posterior distribution. We found that a small percentage ($< 5\%$) of the samples at N^{3}LO contained spurious resonances. We discarded these samples and verified that this did not modify the posterior distribution significantly. The MCMC sampling leads to a posterior distribution over the entire parameter space, which at N^{3}LO is a parameter space spanned by the 21 LECs. This posterior can be converted to posteriors over any two-body observable, such as *np* phase shifts.

In Fig. 2, we show our results for the *np* phase shifts in the $^1S_0$ and $^3S_1$-$^3D_1$ partial waves for both the least-squares fit (dashed lines) and the Bayesian fits (solid lines that represent the maximum of the posterior and the bands that correspond to the 95% confidence level (CL) given the definition of uncertainty discussed above). In the top row, we demonstrate the effect of varying the cutoff R_0 at N^{3}LO, i.e. we show results for our interactions N^{3}LO$_{\rm LA}$-09 to N^{3}LO$_{\rm LA}$-06. In the middle (bottom) row, we vary the chiral EFT order with the cutoff fixed at $R_0 = 0.6$ fm ($R_0 = 0.9$ fm). Figs. 3 and 4 show similar results but for P and D waves respectively. In general, regardless of the cutoff, we find good convergence order-by-order, with our results approaching the NPWA data with reduced uncertainty bands when going to higher orders. By comparing results for different cutoffs, we see that the softer interactions deviate significantly from the

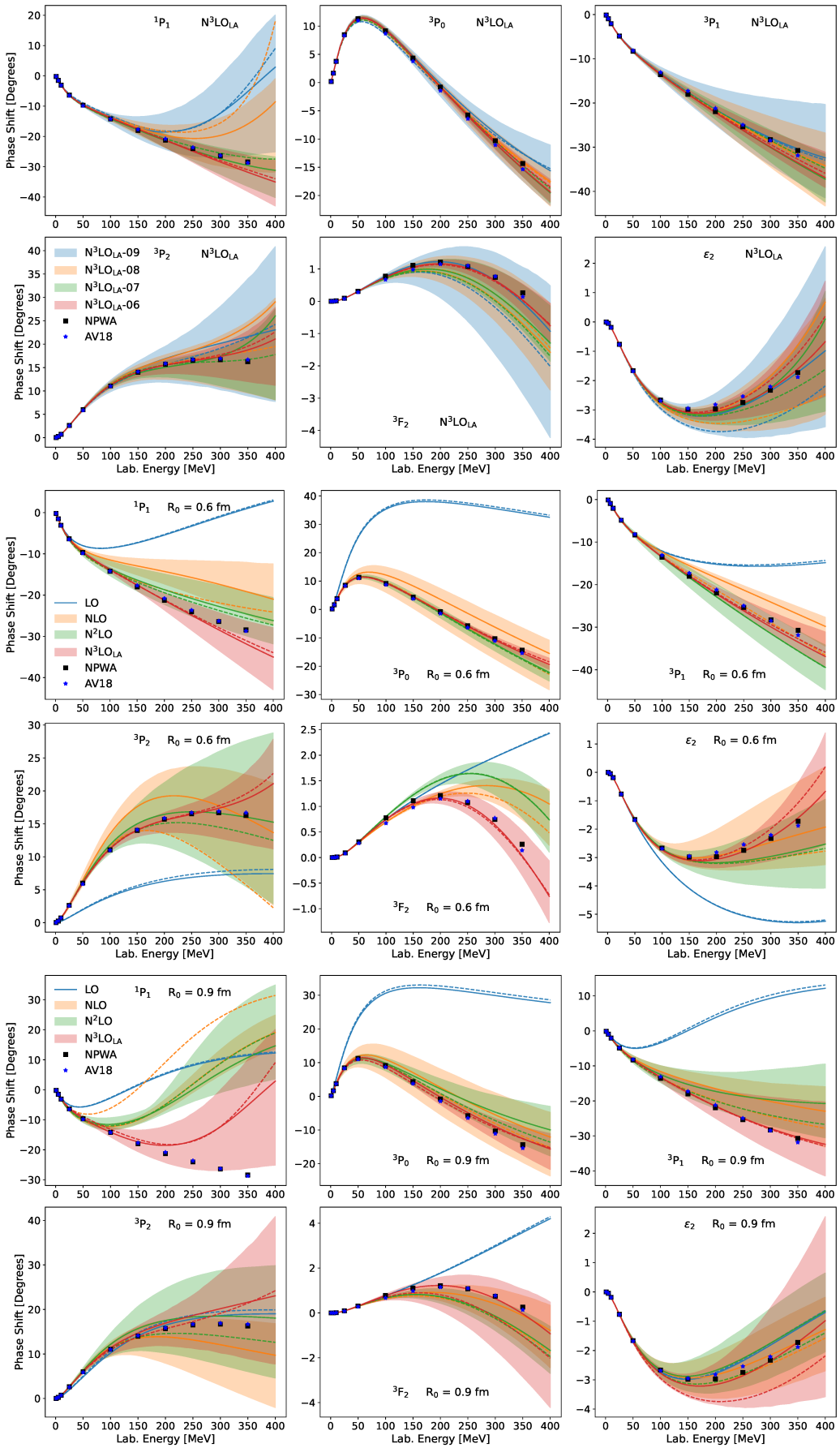

FIG. 3. Similar to Fig. 2, but for the $^1P_1$, $^3P_0$, $^3P_1$ and $^3P_2$-$^3F_2$ partial waves.

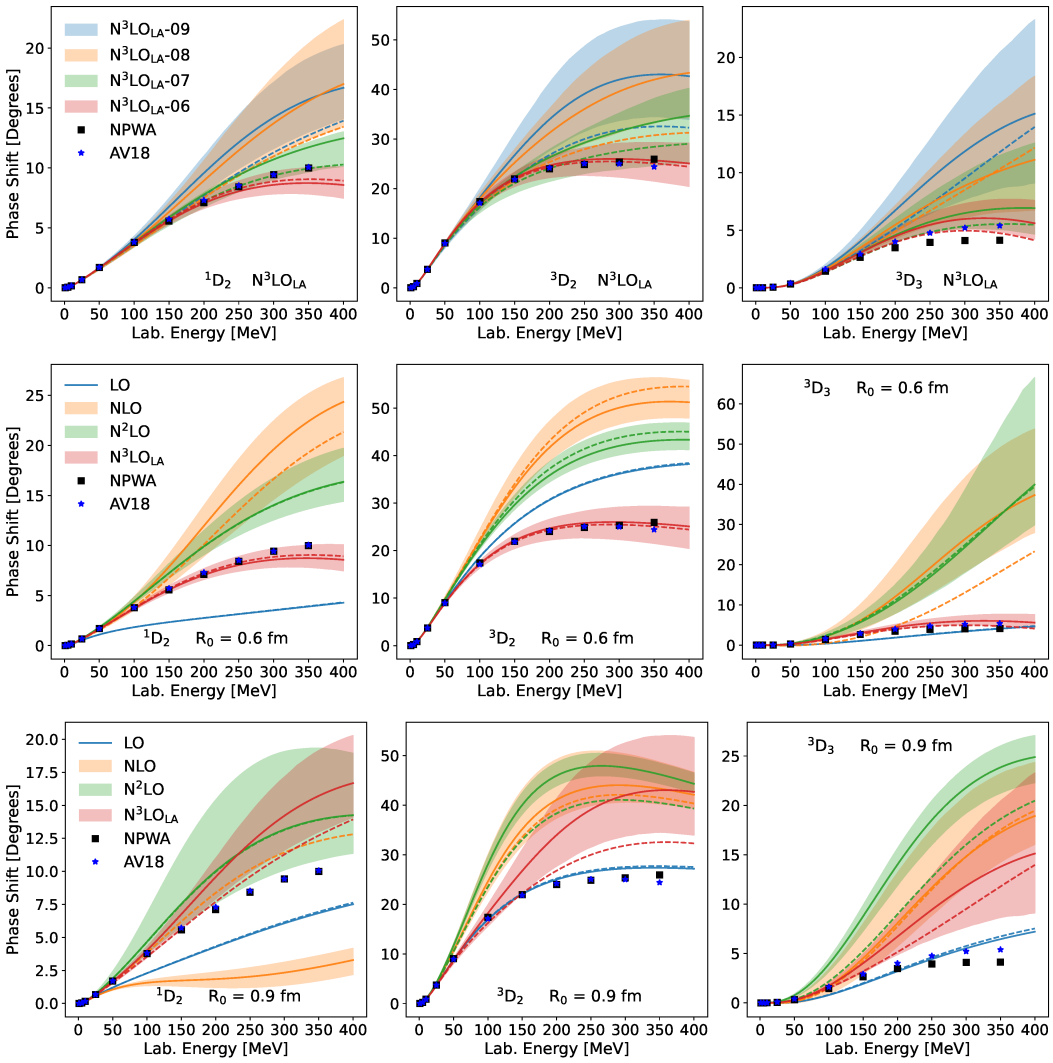

FIG. 4. Similar to Fig. 2, but for the $^1D_2$, $^3D_2$ and $^3D_3$ partial waves.

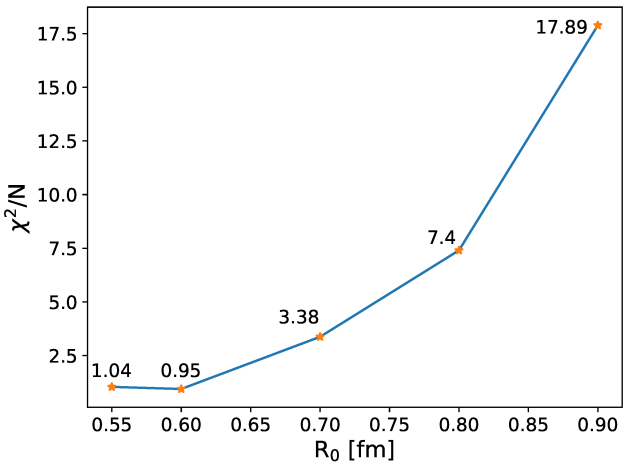

FIG. 5. The objective function defined in Eq. (29) divided by the number of fit parameters N (21 at N^{3}LO) as a function of cutoff for our N^{3}LO$_{\rm LA}$ interactions. The calculated values are written explicitly in the figure.

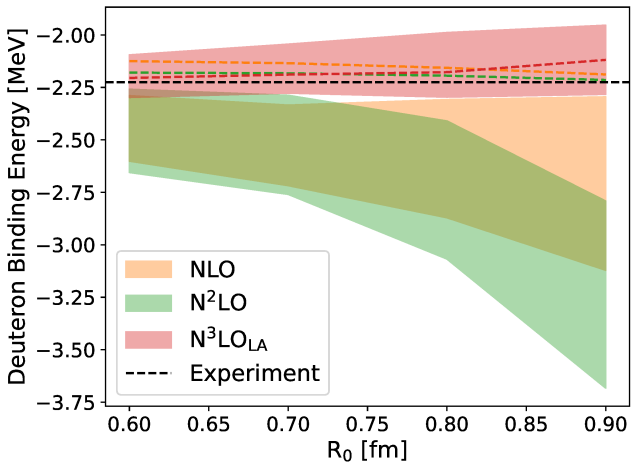

FIG. 6. The deuteron binding energy as a function of cutoff for different orders, as indicated in the legend. The bands correspond to the 95% CL obtained from the Bayesian analysis whereas the dashed lines represent the least-squares results. The dashed black line shows the experimental binding energy.

data at higher lab energies in several partial waves, especially the D waves.

Several comments are in order. First, note the large deviations of the LO phase shifts from the data in almost all channels. This effect enhances the contribution of the LO phase shifts to the EKM uncertainties, which is why it is important to set $X^{\rm LO} = 0$ in Eq. (28) for the fits at N^{3}LO and N^{2}LO. Second, it is important to keep in mind that the uncertainty bands shown here, reflecting the Bayesian posteriors obtained in the fit, are not necessarily the same as the bands obtained following the EKM prescription *a posteriori*. This can be understood by considering a LO interaction where the EKM uncertainties widen with the lab energy due to the almost constant phase shift. However, parts of such an EKM uncertainty band would not be accessible in an actual fit. For example, describing phase shifts that decrease with the lab energy, as provided by the lower bound of an EKM uncertainty band, requires effective-range contributions which are only provided at NLO. Therefore, the results of a Bayesian fit will differ and show a less dramatic energy dependence. Finally, our interactions at lower orders are not fit to the D waves but the N^{3}LO interactions are. As a consequence, the differences between N^{2}LO and N^{3}LO bands in the D waves are larger than the differences between NLO and N^{2}LO.

The impact of the inclusion of the EFT truncation uncertainties that guide the Bayesian fits can be gauged by comparing the solid and dashed lines in all panels in Figs. 2-4. Especially at lower cutoffs, the impact of the EFT truncation uncertainties is important and the Bayesian analysis yields a better reproduction of the data at lower energies as compared to the least-squares fits.

In general, we also find that the high-cutoff interactions give a better reproduction of the NPWA data than low-cutoff interactions, see the top rows in Figs. 2, 3 and 4 where the phase shifts at N^{3}LO are compared for different cutoffs. The Bayesian fits clearly demonstrate the reduction of uncertainty when decreasing R_0, which is equivalent to increasing the momentum-space cutoff Λ_c. In order to stress this point, in Fig. 5 we show the objective function defined in Eq.(29) divided by the number of fit parameters (21 at N^{3}LO) as a function of R_0. We see the strong decrease in the χ^2 as interactions become harder, before plateauing and eventually increasing at $R_0 \sim 0.55$ fm.

The LECs that we obtain for our N^{3}LO$_{\rm LA}$ interactions are given in Table. II for both fitting strategies: least-squares fits and Bayesian fits (maximum posterior estimate). Similar results for the LECs at LO, NLO and N^{2}LO are given in Appendix C.

IV. DEUTERON

Finally, we study properties of the deuteron, which can be completely described by the NN interactions developed here. In this work, we do not fit the interactions to reproduce any properties of the deuteron, and instead choose experimental data on deuteron properties as a benchmark for our interactions.

In Fig. 6, we show the deuteron binding energy as a function of cutoff, for different chiral EFT orders. The bands represent the Bayesian posteriors at the 95% CL whereas the least-squares results are shown as dashed lines. We see that, at N^{3}LO, the least-squares results which do not include any theoretical uncertainty estimates are compatible with the predictions obtained from the Bayesian fits. However, for NLO and N^{2}LO, there is a clear difference between the two analyses. This, once

LEC	Maximum posterior estimate				Least-squares fit			
	0.9 fm	0.8 fm	0.7 fm	0.6 fm	0.9 fm	0.8 fm	0.7 fm	0.6 fm
C_S [fm^2]	2.371	4.784	13.293	27.649	3.698	5.436	15.28	27.595
C_T [fm^2]	0.785	0.79	2.503	2.304	1.029	0.704	2.552	2.742
C_1 [fm^4]	-0.098	-0.001	0.276	0.365	0.167	0.088	0.416	0.352
C_2 [fm^4]	0.129	0.011	0.032	0.013	0.086	0.003	0.023	0.016
C_3 [fm^4]	0.031	0.009	0.075	0.003	0.013	-0.003	0.077	0.004
C_4 [fm^4]	-0.0	-0.019	0.011	0.03	0.025	-0.019	0.004	0.031
C_5 [fm^4]	-1.765	-2.01	-2.358	-2.231	-2.047	-2.072	-2.309	-2.168
C_6 [fm^4]	0.043	0.07	0.154	0.241	0.118	0.074	0.16	0.291
C_7 [fm^4]	-0.171	-0.15	-0.175	-0.186	-0.217	-0.144	-0.165	-0.179
D_1 [fm^6]	-0.013	0.007	0.019	0.023	-0.009	0.007	0.029	0.023
D_2 [fm^6]	0.01	0.006	0.007	0.008	0.025	0.007	0.01	0.008
D_3 [fm^6]	-0.012	-0.012	-0.006	-0.004	-0.02	-0.017	-0.006	-0.005
D_4 [fm^6]	-0.004	0.0	0.007	0.008	0.009	0.007	0.012	0.009
D_5 [fm^6]	0.111	0.032	-0.01	-0.053	0.148	0.076	0.009	-0.058
D_6 [fm^6]	0.042	0.035	0.026	0.01	-0.037	-0.01	0.001	0.001
D_7 [fm^6]	0.042	0.033	0.031	0.024	0.07	0.036	0.037	0.029
D_8 [fm^6]	-0.051	-0.03	-0.028	-0.019	-0.069	-0.036	-0.032	-0.02
$\tilde{D}_{11}$ [fm^6]	0.005	-0.09	-0.101	-0.092	-0.163	-0.133	-0.12	-0.092
$\tilde{D}_{12}$ [fm^6]	-0.059	-0.009	-0.007	-0.004	-0.064	-0.007	-0.005	-0.006
$\tilde{D}_{13}$ [fm^6]	-0.033	-0.042	-0.036	-0.032	-0.083	-0.044	-0.035	-0.037
$\tilde{D}_{15}$ [fm^6]	-0.001	-0.008	0.005	0.015	0.061	0.037	0.023	0.016

TABLE II. LECs for our N^{3}LO$_{\rm LA}$ interactions for different cutoffs. We give results obtained from the Bayesian analyses (left) and least-squares fits (right). For the former, the quoted LECs correspond to the maximum of the posterior distribution.

again, illustrates the importance of incorporating theoretical uncertainties when EFTs are calibrated to experimental data. Also, note that the uncertainties decrease significantly with the chiral order as well as when decreasing R_0, which is consistent with our results for the phase shifts. Our N^{3}LO$_{\rm LA}$ interactions reproduce the experimental deuteron binding energy within theoretical uncertainties for all considered cutoffs.

In Fig. 7, we show results for the deuteron wave function. In the top row, we show the coordinate space wavefunction in the S-wave $\psi_{L=0}(r)$ and D-wave $\psi_{L=2}(r)$. Note that these wavefunctions are related to their components $u(r)$ and $w(r)$, which are sometimes reported in the literature [15, 36, 39], as $\psi_{L=0}(r) = u(r)/r$ and $\psi_{L=2}(r) = w(r)/r$. In the bottom row, we show the momentum-space representation of the wavefunctions in the S-wave $\tilde{\psi}_{L=0}(p)$ and D-wave $\tilde{\psi}_{L=2}(p)$, showing the squared momentum-space wavefunctions in a logarithmic scale. As our fitting code is written in momentum space, we first solve for the momentum-space wavefunctions and then obtain the coordinate-space representations as,

$$\psi_{L=0}(r) = \sqrt{\frac{2}{\pi}} \int_0^\infty dp p^2 j_0(pr) \tilde{\psi}_{L=0}(p), \qquad (30)$$

$$\psi_{L=2}(r) = \sqrt{\frac{2}{\pi}} \int_0^\infty dp p^2 j_2(pr) \tilde{\psi}_{L=2}(p)\,. \qquad (31)$$

In coordinate space, our models do not contain any oscillations in the wave function at intermediate or large r, unlike some chiral interactions developed in the past [38, 39]. Interactions at different cutoffs are identical at large r but have different small-r behavior. In the D-wave, the harder interactions, i.e. N^{3}LO$_{\rm LA}$-06 and N^{3}LO$_{\rm LA}$-07, lead to more pronounced peaks as compared to their softer counterparts N^{3}LO$_{\rm LA}$-08 and N^{3}LO$_{\rm LA}$-09. In momentum space, we see that the harder interactions generally have a more significant high-momentum tail which could have implications for the description of electron scattering experiments [48].

We have used the deuteron wave functions at N^{3}LO to calculate other deuteron observables, which we show in Table III. We give results for both our Bayesian fits (at

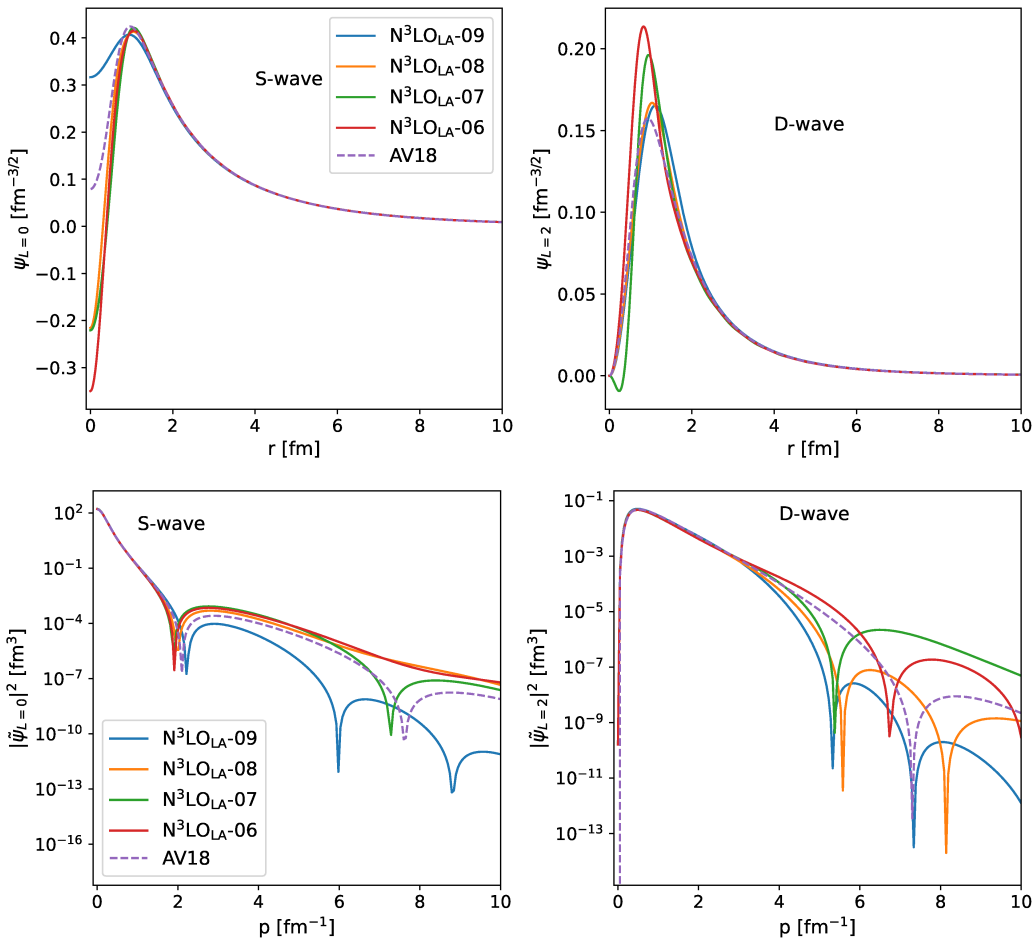

FIG. 7. The deuteron wavefunction in coordinate space (top row) and momentum space (bottom row). The different colors (showing results for different R_0) correspond to the least-squares phase shifts analyses. The dashed line represents the AV18 [42] analysis and is shown as a reference.

the 95% CL) and least-squares fits. For the Bayesian fits, our results are in good agreement with the experimental data within theoretical uncertainties, except for the quadrupole moment. Note that the agreement between the median model predictions and the experiment is better for interactions with smaller coordinate space cutoffs. Furthermore, these harder interactions have smaller uncertainties, similar to what was observed in the phase shift analyses. The least-squares results are also in good agreement with the experimental data, and the agreement improves for harder interactions. Note that our interactions result in D-state probabilities $P_d \gtrsim 6\%$, which is larger that what has been found for other local N^{3}LO interactions [15, 17].

V. SUMMARY AND OUTLOOK

We have constructed maximally local interactions at N^{3}LO in the delta-less version of chiral EFT. Our interactions include a total of 21 contact operators at N^{3}LO, out of which four are nonlocal. We have also included all pion-exchange contributions consistently up to N^{3}LO. We have employed the method of Bayesian statistics in order to calibrate our maximally local interactions to *np* phase shifts, explicitly taking into account EFT truncation uncertainties. We have demonstrated the importance of incorporating these uncertainties in the fit. Finally, we have explored a range of cutoffs that is significantly larger than what is typically explored in the literature, showing explicitly that high-cutoff interactions ($\Lambda_c \sim 660$ MeV) lead to smaller EFT truncation errors and a better reproduction of experimental data. Furthermore, it is expected that these interactions drastically reduce uncertainties due to the violation of the FRF, particularly from three-nucleon interactions [21]. We will demonstrate this explicitly in a forthcoming publication.

Future QMC calculations using the interactions developed in this work will allow us to reduce theoretical uncertainties for atomic nuclei and dense nuclear matter, which is important to improve nuclear-physics inputs to analyses of multi-messenger observations of NSs, and

Observable	Bayesian fit				Least-squares fit				Experiment
	0.9 fm	0.8 fm	0.7 fm	0.6 fm	0.9 fm	0.8 fm	0.7 fm	0.6 fm	
E_d [MeV]	$-2.1^{+0.2}_{-0.2}$	$-2.1^{+0.1}_{-0.2}$	$-2.2^{+0.1}_{-0.1}$	$-2.2^{+0.1}_{-0.1}$	-2.119	-2.177	-2.189	-2.205	-2.224575(9)
Q_d [fm^2]	$0.270^{+0.005}_{-0.005}$	$0.268^{+0.004}_{-0.005}$	$0.268^{+0.004}_{-0.004}$	$0.268^{+0.003}_{-0.003}$	0.278	0.269	0.265	0.264	0.2859(3)
η_d	$0.024^{+0.002}_{-0.002}$	$0.024^{+0.002}_{-0.002}$	$0.024^{+0.001}_{-0.001}$	$0.025^{+0.001}_{-0.001}$	0.0247	0.0244	0.0241	0.0233	0.0256(4)
$\sqrt{\langle r^2\rangle^d_m}$ [fm]	$1.97^{+0.06}_{-0.06}$	$1.99^{+0.05}_{-0.05}$	$1.98^{+0.04}_{-0.04}$	$1.97^{+0.03}_{-0.03}$	1.983	1.975	1.973	1.97	1.9753(11)
A_S [fm$^{-1/2}$]	$0.85^{+0.03}_{-0.03}$	$0.87^{+0.03}_{-0.02}$	$0.87^{+0.02}_{-0.02}$	$0.88^{+0.02}_{-0.02}$	0.860	0.875	0.878	0.882	0.8846(9)
P_d [%]	$6.5^{+0.8}_{-0.8}$	$6.0^{+0.7}_{-0.6}$	$6.3^{+0.5}_{-0.5}$	$6.1^{+0.4}_{-0.4}$	6.64	6.00	6.16	6.26	—

TABLE III. The properties of the deuteron for our N^{3}LO$_{\rm LA}$ interactions, for different cutoffs. For the Bayesian fit, the error bars are quoted at the 95% CL. Here, E_d is the binding energy, Q_d is the quadrupole moment, η_d is the asymptotic D/S ratio, $\sqrt{\langle r^2\rangle^d_m}$ is the root-mean-square matter radius, A_S is the asymptotic S-wave normalization and P_d is the D-state probability.

related simulations. Our results will enable astrophysical tests of nuclear physics models under conditions that cannot be attained in any terrestrial experiment. Moreover, our calculations will provide valuable theoretical benchmarks for nuclear experiments measuring, e.g., the neutron-skin thickness of nuclei (CREX and PREX) or the nuclear symmetry energy (FRIB). The present LIGO observing run, that started in May 2023, and future nuclear experiments at FRIB emphasize the ideal timing for these studies.

ACKNOWLEDGMENTS

We thank Joe Carlson, Stefano Gandolfi, Joshua Martin, Sam Novario, and Ronen Weiss for useful discussions. R.S. acknowledges support from the Nuclear Physics from Multi-Messenger Mergers (NP3M) Focused Research Hub which is funded by the National Science Foundation under Grant Number 21-16686, and by the Laboratory Directed Research and Development program of Los Alamos National Laboratory under project number 20220541ECR. The work of J.E.L., L.H., and A.S. was supported by the European Research Council (ERC) Grant No. 307986 STRONGINT and under the European Union's Horizon 2020 research and innovation programme (Grant Agreement No. 101020842). I.T. was supported by the U.S. Department of Energy, Office of Science, Office of Nuclear Physics, under contract No. DE-AC52-06NA25396, by the Laboratory Directed Research and Development program of Los Alamos National Laboratory under project number 20220541ECR, and by the U.S. Department of Energy, Office of Science, Office of Advanced Scientific Computing Research, Scientific Discovery through Advanced Computing (SciDAC) NUCLEI program.

Appendix A: Fourier transformations of local N^{3}LO contact operators

In this appendix, we give the coordinate-space representation of the local operators quoted in Eq. (6). We construct the Fourier transformation for typical regulators of the form $f(r) = a\exp(-(r/R_0)^n)$; see Sec. II C for the specific value of a and n used in this work.

1. Local operators $\sim q$: D_1 - D_4

Let us denote by $V_{\tau,\sigma}$ the part of the operator that contains the spin-isospin operator structures (momentum-independent part) as well as the LEC. Then, the operators proportional to D_1 - D_4 (see Eq. (6)) have the form $V_{\tau,\sigma}\cdot q^4$. Upon Fourier transformation, we find

$$V_{\tau,\sigma}\Delta^2\delta_{R_0}(\boldsymbol{r}) = n\left[-\frac{(n+1)(n-1)(n-2)r^{n-4}}{R_0^n} + \frac{n(7n+1)(n-1)r^{2n-4}}{R_0^{2n}} - \frac{2n^2(3n-1)r^{3n-4}}{R_0^{3n}} + \frac{n^3r^{4n-4}}{R_0^{4n}}\right] a\exp(-(r/R_0)^n)\,. \tag{A1}$$

2. Local operators $\sim q^2 \boldsymbol{L}\cdot\boldsymbol{S}$: D_5 and D_6

We now transform the N^{3}LO spin-orbit term $V_\tau i\boldsymbol{q}^2(\boldsymbol{\sigma}_1+\boldsymbol{\sigma}_2)\cdot(\boldsymbol{q}\times\boldsymbol{k})$ with $\boldsymbol{S}=\boldsymbol{\sigma}_1+\boldsymbol{\sigma}_2$. As in the NLO case [14], we employ the test function $|\psi\rangle$:

$$
\begin{aligned}
\langle \boldsymbol{r}|\,\hat{O}^{(4)}_{\rm LS}\,|\psi\rangle &= \int\frac{d^3p}{(2\pi)^3}\frac{d^3p'}{(2\pi)^3}d^3r' e^{i\boldsymbol{p}'\cdot\boldsymbol{r}}e^{-i\boldsymbol{p}\cdot\boldsymbol{r}'}\,\langle\boldsymbol{p}'|\,\hat{O}_{\rm LS}\,|\boldsymbol{p}\rangle\,\psi(\boldsymbol{r}') \\
&= iV_\tau\int\frac{d^3q}{(2\pi)^3}\frac{d^3k}{(2\pi)^3}d^3r'\boldsymbol{q}^2\boldsymbol{S}\cdot(\boldsymbol{q}\times\boldsymbol{k})\,e^{i\frac{\boldsymbol{q}}{2}\cdot(\boldsymbol{r}+\boldsymbol{r}')}e^{i\boldsymbol{k}\cdot(\boldsymbol{r}-\boldsymbol{r}')}\psi(\boldsymbol{r}')f(q^2) \\
&= iV_\tau\int\frac{d^3q}{(2\pi)^3}\frac{d^3k}{(2\pi)^3}d^3r'\boldsymbol{q}^2\epsilon^{abc}S_aq_bk_c\,e^{i\frac{\boldsymbol{q}}{2}\cdot(\boldsymbol{r}+\boldsymbol{r}')}e^{i\boldsymbol{k}\cdot(\boldsymbol{r}-\boldsymbol{r}')}\psi(\boldsymbol{r}')f(q^2) \\
&= iV_\tau\int\frac{d^3q}{(2\pi)^3}\frac{d^3k}{(2\pi)^3}d^3r'\boldsymbol{q}^2\epsilon^{abc}S_aq_b\,e^{i\frac{\boldsymbol{q}}{2}\cdot(\boldsymbol{r}+\boldsymbol{r}')}\left(i\partial'_ce^{i\boldsymbol{k}\cdot(\boldsymbol{r}-\boldsymbol{r}')}\right)\psi(\boldsymbol{r}')f(q^2) \\
&\overset{p.i.}{=} -iV_\tau\int\frac{d^3q}{(2\pi)^3}\frac{d^3k}{(2\pi)^3}d^3r'\boldsymbol{q}^2\epsilon^{abc}S_aq_b\,\left(i\partial'_ce^{i\frac{\boldsymbol{q}}{2}\cdot\boldsymbol{r}'}\psi(\boldsymbol{r}')\right)e^{i\boldsymbol{k}\cdot(\boldsymbol{r}-\boldsymbol{r}')}f(q^2)e^{i\frac{\boldsymbol{q}}{2}\cdot\boldsymbol{r}} \\
&= -iV_\tau\int\frac{d^3q}{(2\pi)^3}\boldsymbol{q}^2\epsilon^{abc}S_aq_b\,\left(i\partial_ce^{i\frac{\boldsymbol{q}}{2}\cdot\boldsymbol{r}}\psi(\boldsymbol{r})\right)f(q^2)e^{i\frac{\boldsymbol{q}}{2}\cdot\boldsymbol{r}} \\
&= -iV_\tau\int\frac{d^3q}{(2\pi)^3}\boldsymbol{q}^2\epsilon^{abc}S_aq_b\,\left(i\partial_c\psi(\boldsymbol{r})\right)f(q^2)e^{i\boldsymbol{q}\cdot\boldsymbol{r}} \qquad \text{(antisymmetry of } \epsilon) \\
&= -V_\tau\epsilon^{abc}S_a\partial_b\left(\int\frac{d^3q}{(2\pi)^3}\boldsymbol{q}^2\,f(q^2)e^{i\boldsymbol{q}\cdot\boldsymbol{r}}\right)(i\partial_c\psi(\boldsymbol{r})) \\
&= -V_\tau\epsilon^{abc}S_a\partial_b\left(\Delta\delta_{R_0}\right)(i\partial_c\psi(\boldsymbol{r})) = -V_\tau\epsilon^{abc}S_a\partial_b\left(\frac{2\partial_r\delta_{R_0}}{r}+\partial_r^2\delta_{R_0}\right)(i\partial_c\psi(\boldsymbol{r})) \\
&= V_\tau\left(\frac{\partial_r^3\delta_{R_0}}{r}+\frac{2\partial_r^2\delta_{R_0}}{r^2}-\frac{2\partial_r\delta_{R_0}}{r^3}\right)\boldsymbol{L}\cdot\boldsymbol{S}\psi(\boldsymbol{r})\,.
\end{aligned}
\tag{A2}
$$

3. Local operators $\sim q^2 S_{12}$: D_7 and D_8

Next, we FT the tensor operators of the form $V_\tau\,\boldsymbol{q}^2\boldsymbol{\sigma}_1\cdot\boldsymbol{q}\,\boldsymbol{\sigma}_2\cdot\boldsymbol{q}$:

$$
\begin{aligned}
&\int\frac{d^3q}{(2\pi)^3}\,f(q^2)V_\tau\,\boldsymbol{q}^2\boldsymbol{\sigma}_1\cdot\boldsymbol{q}\,\boldsymbol{\sigma}_2\cdot\boldsymbol{q}\,e^{i\boldsymbol{q}\cdot\boldsymbol{r}} \\
&= V_\tau\sigma_1^i\sigma_2^j\partial_a\partial_a\partial_i\partial_j\int\frac{d^3q}{(2\pi)^3}\,f(q^2)\,e^{i\boldsymbol{q}\cdot\boldsymbol{r}} = V_\tau\sigma_1^i\sigma_2^j\partial_a\partial_a\partial_i\partial_j\delta_{R_0}(\boldsymbol{r}) \\
&= V_\tau\sigma_1^i\sigma_2^j\partial_i\partial_j\left(\frac{2\partial_r\delta_{R_0}(\boldsymbol{r})}{r}+\partial_r^2\delta_{R_0}(\boldsymbol{r})\right) \\
&= V_\tau\sigma_1^i\sigma_2^j\partial_i\left(r_j\frac{2\partial_r^2\delta_{R_0}(\boldsymbol{r})}{r^2}-r_j\frac{2\partial_r\delta_{R_0}(\boldsymbol{r})}{r^3}+r_j\frac{\partial_r^3\delta_{R_0}(\boldsymbol{r})}{r}\right) \\
&= V_\tau\sigma_1^i\sigma_2^j\left(\delta^{ij}\left(\frac{\partial_r^3\delta_{R_0}(\boldsymbol{r})}{r}+\frac{2\partial_r^2\delta_{R_0}(\boldsymbol{r})}{r^2}-\frac{2\partial_r\delta_{R_0}(\boldsymbol{r})}{r^3}\right)\right. \\
&\quad\left.+r_ir_j\left(\frac{\partial_r^4\delta_{R_0}(\boldsymbol{r})}{r^2}+\frac{\partial_r^3\delta_{R_0}(\boldsymbol{r})}{r^3}-\frac{6\partial_r^2\delta_{R_0}(\boldsymbol{r})}{r^4}+\frac{6\partial_r\delta_{R_0}(\boldsymbol{r})}{r^5}\right)\right) \\
&= V_\tau\left(\boldsymbol{\sigma}_1\cdot\boldsymbol{\sigma}_2\left(\frac{\partial_r^3\delta_{R_0}(\boldsymbol{r})}{r}+\frac{2\partial_r^2\delta_{R_0}(\boldsymbol{r})}{r^2}-\frac{2\partial_r\delta_{R_0}(\boldsymbol{r})}{r^3}\right)\right. \\
&\quad\left.+3\,\boldsymbol{\sigma}_1\cdot\hat{\boldsymbol{r}}\,\boldsymbol{\sigma}_2\cdot\hat{\boldsymbol{r}}\left(\frac{\partial_r^4\delta_{R_0}(\boldsymbol{r})}{3}+\frac{\partial_r^3\delta_{R_0}(\boldsymbol{r})}{3r}-\frac{2\partial_r^2\delta_{R_0}(\boldsymbol{r})}{r^2}+\frac{2\partial_r\delta_{R_0}(\boldsymbol{r})}{r^3}\right)\right)\,.
\end{aligned}
\tag{A3}
$$

Appendix B: Testing different sets of nonlocal operators

In this work, we have chosen a set of four nonlocal operators specified in Eq. (18), leading to the construction of the interactions N^{3}LO$_{\rm LA}$-09 to N^{3}LO$_{\rm LA}$-06. However,

as discussed in Sec. II B 1, other choices for these nonlocal pieces are possible due to FRF and the freedom in choosing the parameters of the UT. In this appendix, we will briefly investigate four other possible sets of nonlocal operators, with the cutoff fixed at $R_0 = 0.9$ fm, and comapre them with $\mathrm{N^3LO_{LA}}$-09.

The alternative sets, Set 1 to Set 4, are defined by the choice of 4 nonlocal operators as follows:

$$\begin{aligned} V_{\text{Set 1}} = {} & \tilde{D}_9\, \boldsymbol{q}^2\boldsymbol{k}^2 + \tilde{D}_{10}\, \boldsymbol{q}^2\boldsymbol{k}^2 \boldsymbol{\tau}_1\cdot\boldsymbol{\tau}_2 \\ & + \tilde{D}_{13}\, \boldsymbol{k}^2\, \boldsymbol{\sigma}_1\cdot\boldsymbol{q}\, \boldsymbol{\sigma}_2\cdot\boldsymbol{q} \\ & + \tilde{D}_{15}\, (\boldsymbol{\sigma}_1\cdot\boldsymbol{L})(\boldsymbol{\sigma}_2\cdot\boldsymbol{L})\,, \end{aligned} \tag{B1}$$

$$\begin{aligned} V_{\text{Set 2}} = {} & \tilde{D}_9\, \boldsymbol{q}^2\boldsymbol{k}^2 + \tilde{D}_{12}\, \boldsymbol{L}^2 \boldsymbol{\tau}_1\cdot\boldsymbol{\tau}_2 \\ & + \tilde{D}_{13}\, \boldsymbol{k}^2\, \boldsymbol{\sigma}_1\cdot\boldsymbol{q}\, \boldsymbol{\sigma}_2\cdot\boldsymbol{q} \\ & + \tilde{D}_{15}\, (\boldsymbol{\sigma}_1\cdot\boldsymbol{L})(\boldsymbol{\sigma}_2\cdot\boldsymbol{L})\,, \end{aligned} \tag{B2}$$

$$\begin{aligned} V_{\text{Set 3}} = {} & \tilde{D}_{10}\, \boldsymbol{q}^2\boldsymbol{k}^2 \boldsymbol{\tau}_1\cdot\boldsymbol{\tau}_2 + \tilde{D}_{11}\, \boldsymbol{L}^2 \\ & + \tilde{D}_{13}\, \boldsymbol{k}^2\, \boldsymbol{\sigma}_1\cdot\boldsymbol{q}\, \boldsymbol{\sigma}_2\cdot\boldsymbol{q} \\ & + \tilde{D}_{15}\, (\boldsymbol{\sigma}_1\cdot\boldsymbol{L})(\boldsymbol{\sigma}_2\cdot\boldsymbol{L})\,, \end{aligned} \tag{B3}$$

$$\begin{aligned} V_{\text{Set 4}} = {} & \tilde{D}_{11}\, \boldsymbol{L}^2 + \tilde{D}_{12}\, \boldsymbol{L}^2 \boldsymbol{\tau}_1\cdot\boldsymbol{\tau}_2 \\ & + \tilde{D}_{14}\, \boldsymbol{k}^2\, \boldsymbol{\sigma}_1\cdot\boldsymbol{q}\, \boldsymbol{\sigma}_2\cdot\boldsymbol{q}\boldsymbol{\tau}_1\cdot\boldsymbol{\tau}_2 \\ & + \tilde{D}_{15}\, (\boldsymbol{\sigma}_1\cdot\boldsymbol{L})(\boldsymbol{\sigma}_2\cdot\boldsymbol{L}). \end{aligned} \tag{B4}$$

An important consideration in choosing the operator set is regarding the perturbativeness of the nonlocal pieces, which is important for their application in QMC calculations. In Fig. 8, we show the differences between the phase shifts in several partial waves for these interactions and the predictions with all nonlocal parts set to zero. By examining these differences, we can judge the relative strength of the nonlocal terms, i.e. the extent to which the full solution is determined by the local operators alone. While the question of the perturbativeness of the nonlocal operators depends on the observable in question, this phase shift analysis might already indicate the sets of nonlocal operators that would be best suited for a perturbative treatment in many-body calculations. Generally, all sets perform comparably well, while Set 3 and the $\mathrm{N^3LO_{LA}}$-09 are the only sets giving a reasonable behavior in the $^1\mathrm{P}_1$ partial wave. Set 3 seems to be slightly more perturbative in the P waves but $\mathrm{N^3LO_{LA}}$-09 performs better in the S and D wave channels. This indicates that the choice of nonlocal operators made in this work, Eq. (18), might be well suited for applications to many-body nuclear systems.

Appendix C: Operator LECs at LO, NLO and $\mathrm{N^2LO}$

In this appendix, we give the operator LECs that we have obtained from our phase shifts analyses at LO, NLO and $\mathrm{N^2LO}$. The LECs are quoted in Tables IV, V and VI.

[1] E. Annala, T. Gorda, A. Kurkela, and A. Vuorinen, Phys. Rev. Lett. **120**, 172703 (2018), arXiv:1711.02644 [astro-ph.HE].
[2] Y. Lim and J. W. Holt, Phys. Rev. Lett. **121**, 062701 (2018), arXiv:1803.02803 [nucl-th].
[3] C. D. Capano, I. Tews, S. M. Brown, B. Margalit, S. De, S. Kumar, D. A. Brown, B. Krishnan, and S. Reddy, Nature Astron. **4**, 625 (2020), arXiv:1908.10352 [astro-ph.HE].
[4] E. Annala, T. Gorda, A. Kurkela, J. Nättilä, and A. Vuorinen, Nature Phys. **16**, 907 (2020), arXiv:1903.09121 [astro-ph.HE].
[5] T. Dietrich, M. W. Coughlin, P. T. H. Pang, M. Bulla, J. Heinzel, L. Issa, I. Tews, and S. Antier, Science **370**, 1450 (2020), arXiv:2002.11355 [astro-ph.HE].
[6] R. Essick, P. Landry, A. Schwenk, and I. Tews, Phys. Rev. C **104**, 065804 (2021), arXiv:2107.05528 [nucl-th].
[7] G. Raaijmakers, S. K. Greif, K. Hebeler, T. Hinderer, S. Nissanke, A. Schwenk, T. E. Riley, A. L. Watts, J. M. Lattimer, and W. C. G. Ho, Astrophys. J. Lett. **918**, L29 (2021), arXiv:2105.06981 [astro-ph.HE].
[8] S. Huth *et al.*, Nature **606**, 276 (2022), arXiv:2107.06229 [nucl-th].
[9] E. Epelbaum, H.-W. Hammer, and U.-G. Meissner, Rev. Mod. Phys. **81**, 1773 (2009), arXiv:0811.1338 [nucl-th].
[10] R. Machleidt and D. R. Entem, Phys. Rept. **503**, 1 (2011), arXiv:1105.2919 [nucl-th].
[11] H. W. Hammer, S. König, and U. van Kolck, Rev. Mod. Phys. **92**, 025004 (2020), arXiv:1906.12122 [nucl-th].
[12] J. Carlson, S. Gandolfi, F. Pederiva, S. C. Pieper, R. Schiavilla, K. E. Schmidt, and R. B. Wiringa, Rev. Mod. Phys. **87**, 1067 (2015), arXiv:1412.3081 [nucl-th].
[13] A. Gezerlis, I. Tews, E. Epelbaum, S. Gandolfi, K. Hebeler, A. Nogga, and A. Schwenk, Phys. Rev. Lett. **111**, 032501 (2013), arXiv:1303.6243 [nucl-th].
[14] A. Gezerlis, I. Tews, E. Epelbaum, M. Freunek, S. Gandolfi, K. Hebeler, A. Nogga, and A. Schwenk, Phys. Rev. C **90**, 054323 (2014), arXiv:1406.0454 [nucl-th].
[15] M. Piarulli, L. Girlanda, R. Schiavilla, R. Navarro Pérez, J. E. Amaro, and E. Ruiz Arriola, Phys. Rev. C **91**, 024003 (2015), arXiv:1412.6446 [nucl-th].
[16] M. Piarulli *et al.*, Phys. Rev. Lett. **120**, 052503 (2018), arXiv:1707.02883 [nucl-th].
[17] S. K. Saha, D. R. Entem, R. Machleidt, and Y. Nosyk, Phys. Rev. C **107**, 034002 (2023), arXiv:2209.13170 [nucl-th].
[18] L. Huth, I. Tews, J. E. Lynn, and A. Schwenk, Phys. Rev. C **96**, 054003 (2017), arXiv:1708.03194 [nucl-th].
[19] D. Lonardoni, J. Carlson, S. Gandolfi, J. E. Lynn, K. E. Schmidt, A. Schwenk, and X. Wang, Phys. Rev. Lett. **120**, 122502 (2018), arXiv:1709.09143 [nucl-th].

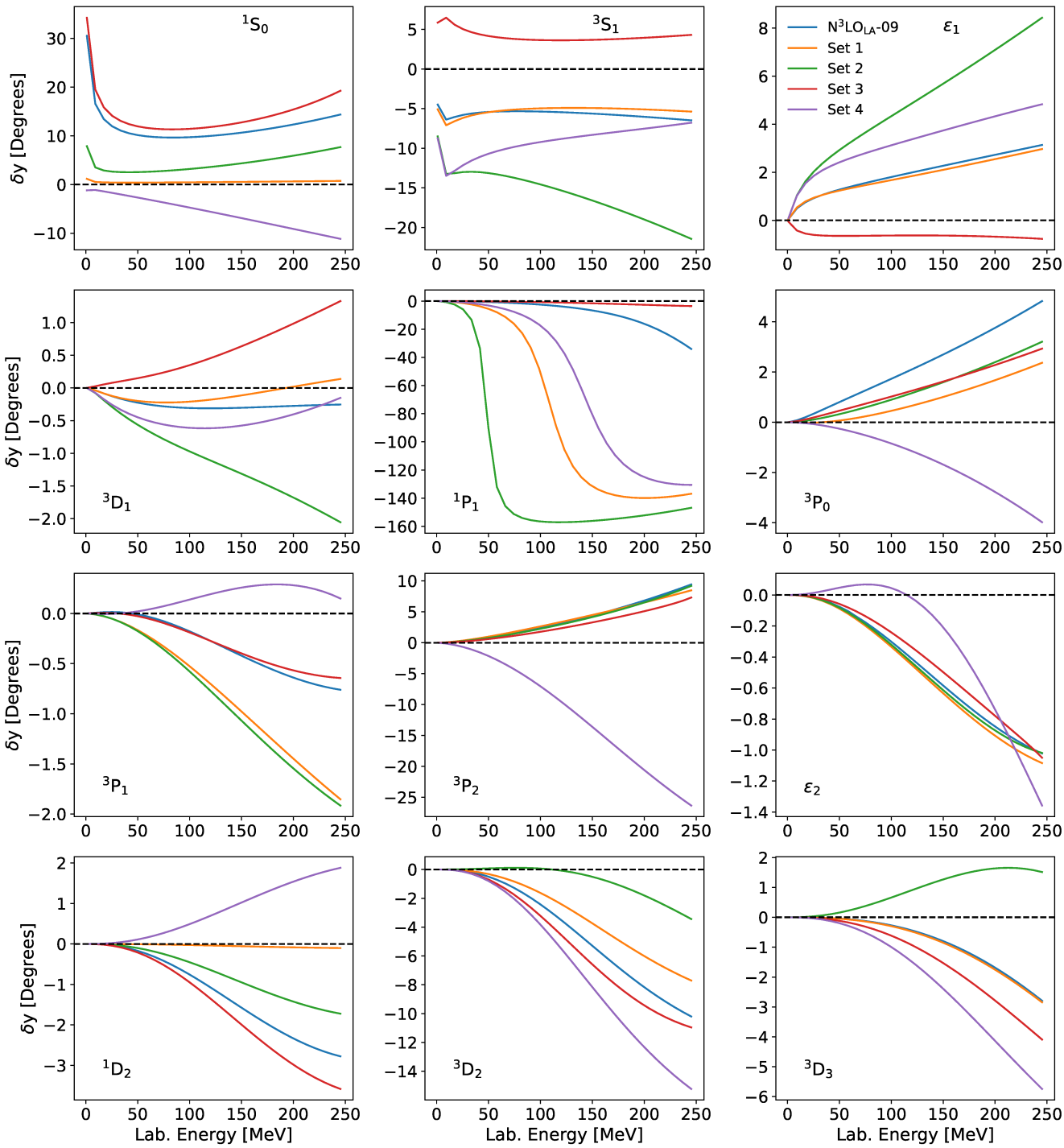

FIG. 8. Differences between the phase shifts obtained using the full interaction and the predictions with all nonlocal parts set to zero. We show results for the N^3LO_{LA}-09 interaction as well as the interactions defined in Eqs. (B2) to (B4), i.e. Set 1 to Set 4.

[20] J. D. Martin, S. J. Novario, D. Lonardoni, J. Carlson, S. Gandolfi, and I. Tews, (2023), arXiv:2301.08349 [nucl-th].

[21] J. E. Lynn, I. Tews, J. Carlson, S. Gandolfi, A. Gezerlis, K. E. Schmidt, and A. Schwenk, Phys. Rev. Lett. **116**, 062501 (2016), arXiv:1509.03470 [nucl-th].

[22] I. Tews, J. Carlson, S. Gandolfi, and S. Reddy, Astrophys. J. **860**, 149 (2018), arXiv:1801.01923 [nucl-th].

[23] D. Lonardoni, I. Tews, S. Gandolfi, and J. Carlson, Phys. Rev. Res. **2**, 022033 (2020), arXiv:1912.09411 [nucl-th].

[24] S. J. Novario, D. Lonardoni, S. Gandolfi, and G. Hagen, Phys. Rev. Lett. **130**, 032501 (2023), arXiv:2111.12775

LEC	Maximum posterior estimate				Least-squares fit			
	0.9 fm	0.8 fm	0.7 fm	0.6 fm	0.9 fm	0.8 fm	0.7 fm	0.6 fm
C_S [fm^2]	0.666	1.971	4.196	8.641	1.299	2.679	4.965	9.157
C_T [fm^2]	0.467	0.508	0.699	1.426	0.684	0.749	0.951	1.607
C_1 [fm^4]	-0.001	-0.05	-0.097	-0.211	-0.057	-0.04	-0.072	-0.172
C_2 [fm^4]	-0.034	0.024	0.035	0.072	0.127	0.096	0.072	0.064
C_3 [fm^4]	-0.093	-0.095	-0.087	-0.096	-0.092	-0.086	-0.081	-0.08
C_4 [fm^4]	0.06	0.073	0.103	0.156	0.112	0.108	0.122	0.151
C_5 [fm^4]	-1.948	-1.991	-2.23	-2.897	-2.158	-2.168	-2.354	-2.948
C_6 [fm^4]	0.303	0.208	0.18	0.196	0.287	0.23	0.2	0.202
C_7 [fm^4]	-0.479	-0.353	-0.308	-0.356	-0.507	-0.406	-0.353	-0.361

TABLE IV. Similar to Table II but at N^{2}LO.

LEC	Maximum posterior estimate				Least-squares fit			
	0.9 fm	0.8 fm	0.7 fm	0.6 fm	0.9 fm	0.8 fm	0.7 fm	0.6 fm
C_S [fm^2]	0.083	0.95	2.576	7.954	0.043	1.503	4.952	17.72
C_T [fm^2]	0.326	0.662	1.045	0.329	0.881	1.082	1.946	5.068
C_1 [fm^4]	0.125	0.598	0.59	0.887	0.256	0.483	0.553	0.848
C_2 [fm^4]	0.095	0.173	0.091	-0.017	0.162	0.24	0.277	0.42
C_3 [fm^4]	0.109	-0.242	-0.11	-0.116	-0.07	-0.169	-0.097	-0.137
C_4 [fm^4]	0.148	0.037	0.043	-0.028	0.128	0.066	0.123	0.275
C_5 [fm^4]	-1.876	-1.948	-2.103	-2.386	-2.22	-2.304	-2.659	-3.713
C_6 [fm^4]	0.367	0.321	0.261	0.132	0.355	0.337	0.393	0.63
C_7 [fm^4]	-0.472	-0.369	-0.277	-0.125	-0.509	-0.432	-0.442	-0.643

TABLE V. Similar to Table II but at NLO.

[nucl-th].

[25] D. Adhikari *et al.* (PREX, CREX), Phys. Rev. Lett. **128**, 142501 (2022), arXiv:2111.04250 [nucl-ex].

[26] B. T. Reed, F. J. Fattoyev, C. J. Horowitz, and J. Piekarewicz, Phys. Rev. Lett. **126**, 172503 (2021), arXiv:2101.03193 [nucl-th].

[27] R. Essick, I. Tews, P. Landry, and A. Schwenk, Phys. Rev. Lett. **127**, 192701 (2021), arXiv:2102.10074 [nucl-th].

[28] D. Finstad, L. V. White, and D. A. Brown, (2022), arXiv:2211.01396 [astro-ph.HE].

[29] V. Bernard, E. Epelbaum, H. Krebs, and U.-G. Meissner, Phys. Rev. C **77**, 064004 (2008), arXiv:0712.1967 [nucl-th].

[30] V. Bernard, E. Epelbaum, H. Krebs, and U. G. Meissner, Phys. Rev. C **84**, 054001 (2011), arXiv:1108.3816 [nucl-th].

[31] C. Drischler, R. J. Furnstahl, J. A. Melendez, and D. R. Phillips, Phys. Rev. Lett. **125**, 202702 (2020), arXiv:2004.07232 [nucl-th].

[32] A. Dyhdalo, R. J. Furnstahl, K. Hebeler, and I. Tews, Phys. Rev. C **94**, 034001 (2016), arXiv:1602.08038 [nucl-th].

[33] E. Epelbaum, H. Krebs, and U. G. Meißner, Eur. Phys. J. A **51**, 53 (2015), arXiv:1412.0142 [nucl-th].

[34] C. Drischler, J. A. Melendez, R. J. Furnstahl, and D. R. Phillips, Phys. Rev. C **102**, 054315 (2020), arXiv:2004.07805 [nucl-th].

[35] D. R. Entem, R. Machleidt, and Y. Nosyk, Phys. Rev. C **96**, 024004 (2017), arXiv:1703.05454 [nucl-th].

[36] P. Reinert, H. Krebs, and E. Epelbaum, Eur. Phys. J. A **54**, 86 (2018), arXiv:1711.08821 [nucl-th].

[37] I. Tews, S. Gandolfi, A. Gezerlis, and A. Schwenk, Phys. Rev. C **93**, 024305 (2016), arXiv:1507.05561 [nucl-th].

[38] D. R. Entem and R. Machleidt, Phys. Rev. C **68**, 041001 (2003), arXiv:nucl-th/0304018.

[39] E. Epelbaum, W. Glockle, and U.-G. Meissner, Nucl. Phys. A **747**, 362 (2005), arXiv:nucl-th/0405048.

[40] A. Ekström, G. R. Jansen, K. A. Wendt, G. Hagen, T. Papenbrock, B. D. Carlsson, C. Forssén, M. Hjorth-Jensen, P. Navrátil, and W. Nazarewicz, Phys. Rev. C **91**, 051301 (2015), arXiv:1502.04682 [nucl-th].

[41] S. Wesolowski, R. Furnstahl, J. Melendez, and D. Phillips, J. Phys. G **46**, 045102 (2019), arXiv:1808.08211 [nucl-th].

LEC	Maximum posterior estimate				Least-squares fit			
	0.9 fm	0.8 fm	0.7 fm	0.6 fm	0.9 fm	0.8 fm	0.7 fm	0.6 fm
C_S [fm^2]	-2.527	-1.983	-1.38	-0.634	-2.627	-2.074	-1.464	-0.712
C_T [fm^2]	-0.061	0.029	0.141	0.302	-0.08	0.013	0.126	0.287

TABLE VI. Similar to Table II but at LO.

[42] R. B. Wiringa, V. G. J. Stoks, and R. Schiavilla, Phys. Rev. C **51**, 38 (1995), arXiv:nucl-th/9408016.

[43] M. Hoferichter, J. Ruiz de Elvira, B. Kubis, and U.-G. Meißner, Phys. Rept. **625**, 1 (2016), arXiv:1510.06039 [hep-ph].

[44] V. G. J. Stoks, R. A. M. Klomp, M. C. M. Rentmeester, and J. J. de Swart, Phys. Rev. C **48**, 792 (1993).

[45] F. L. Huth, *Local interactions and shell-model interactions from chiral effective field theory*, Ph.D. thesis, Technische Universität Darmstadt (2018).

[46] J. Keller, C. Wellenhofer, K. Hebeler, and A. Schwenk, Phys. Rev. C **103**, 055806 (2021), arXiv:2011.05855 [nucl-th].

[47] I. Svensson, A. Ekström, and C. Forssén, (2023), arXiv:2304.02004 [nucl-th].

[48] A. Schmidt *et al.* (CLAS), Nature **578**, 540 (2020), arXiv:2004.11221 [nucl-ex].